A RESISTIVE TOMOGRAPHY ALGORITHM

by

BRADLEY FRY

A thesis
presented to the University of Manitoba
in partial fulfillment of the
requirements for the degree of
MASTER OF SCIENCE
in
ELECTRICAL ENGINEERING

Winnipeg, Manitoba, 1983

A RESISTIVE TOMOGRAPHY ALGORITHM

BY

BRADLEY FRY

A thesis submitted to the Faculty of Graduate Studies of the University of Manitoba in partial fulfillment of the requirements of the degree of

MASTER OF SCIENCE

ABSTRACT

A new method is presented for reconstructing distributions of electrical conductivity from sets of potential measurements taken over the boundaries.

The reconstruction process involves the solution of a nonlinear system of equations generated by finite element discretization. The method presented decouples the nonlinear system into three linear subsystems which are then solved simultaneously using either a point-iterative successive overrelaxation method or a combination of point-iterative and pre-conditioned conjugate gradient methods. The technique obtains the best conductivity distribution -- in the least-squares sense -- from simulated or measured data.

The conductivity inversion recovery procedure is applied to both two and three-dimensional field problems, as well as to resistance networks, and example solutions are presented.

ACKNOWLEDGEMENTS

The author wishes to thank Professor A. Wexler, both advisor and good friend, for his guidance, encouragement, and patience throughout the duration of this project. It is due primarily to his vision and persistence that this work enjoys the success achieved thus far.

The main ideas of impedance imaging, at the University of Manitoba, were initially explored by Professor Wexler. Subsequently, Mr. B. W. Gawick and Dr. M. Friedman became involved. The work of Mr. Gawick clearly demonstrated the feasibility and validity of the imaging concept. Later, Mr. J. G. Shaw and the author collaborated during the development of the point-iterative algorithm for scalar field solutions.

The author especially wishes to acknowledge the advice, suggestions, and counsel of colleagues within the Numerical Applications Group in the Department of Electrical Engineering. In particular, Mr. R. L. Nakonechny and Mr. M. J. Van der Tol are thanked for their contibutions to the various image display implementations. Mr. Nakonechny warrants a special acknowledgement for his efforts in writing the preconditioned conjugate gradient routines as well as for his assistance during the implementation of the resistive imag-

ing algorithm. Also, Mr. N. M. Stern and Mr. B. W. Klimpke are thanked for their efforts at realizing preliminary hardware prototypes of an automated potential measuring device. As well, Mr. S. Bilgen, Mr. Y. B. Yildir, and Mr. M. H. Lean are thanked for their patience and cooperation during discussions pertaining to more theoretical aspects of field theory and variational methods.

Financial support from the National Research Council and the Department of National Defence, Suffield, Alberta is gratefully acknowledged.

CONTENTS

LIST OF TABLES

LIST OF FIGURES

Chapter I

INTRODUCTION

Most imaging methods seek to reconstruct the interior of a region from sets of measurements taken either throughout the region or over the boundaries of the region. Various means of accomplishing the reconstruction have been proposed, and a number of devices have been developed to exploit each technique.

Chapter I briefly discusses some of the more common imaging processes and attempts to highlight the main problem areas for each. Chapter II provides background information relating to an alternative method, Impedance Computed Tomography (ICT). It also reviews basic ICT concepts; lists reasons for preferring ICT over other methods in certain applications; describes perceived areas of useage; and surveys relevant literature. Chapter III presents a new method for reconstructing interior network resistance values from sets of voltage measurements taken only at accessible network nodes. Chapter IV, in a fashion that parallels the network algorithm development, presents a novel technique for reconstructing distributions of electrical conductivity from sets of potential measurements taken only over the boundaries. Results of computer simulations are discussed throughout.

Finally, in addition to discussing recovered image quality, Chapter V explores the question of excitation requirements and points out possible effects due to modelling errors.

1.1 X-RAY IMAGING

The most common reconstruction methods are found in X-ray tomography, where it is desired to recover the interior of a body cross-section from sets of X-ray absorbtion measurements. As in Fig. 1.1 the beam source and detector are placed on opposite sides of the body and moved in tandem for a prescribed number of intervals.

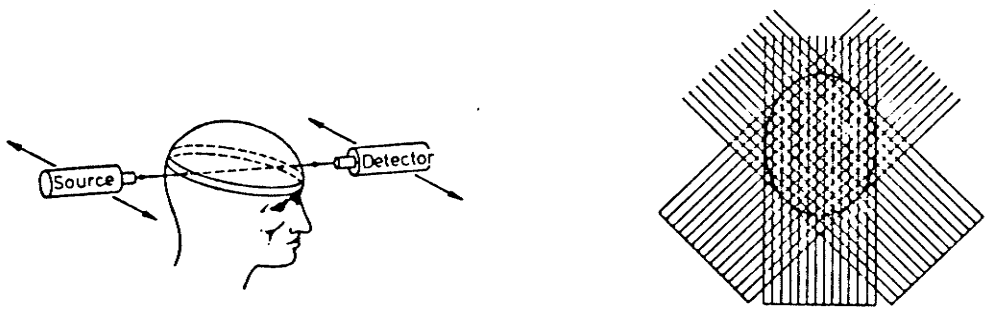

Figure 1.1: X-Ray Scanning Method.
(From Brooks and Di Chiro [3])

At each interval the beam traverses the straight line (i.e. ray-path) between source and detector, and suffers some measureable loss of energy due to the attenuation coeffi-

cient $\mu(x,y)$ of the media. Different body organs will have different attenuation factors due to variations in tissue density and atomic number [1]. The transmitted beam intensity is given by

$$I = I_o \exp[-\int \mu(x,y)ds] \qquad (1.1)$$

where I_o is the incident beam intensity.

The integral of the attenuation function along the ray-path is known as the ray-projection p, and from (1.1) is

$$p = -\ell n(I/I_o). \qquad (1.2)$$

A complete set of ray-projections at a given angle constitute a single projection. More projections are obtained by repeating ray-projection measurements for as many angles as necessary. In principle, an infinite number of projections are required to reconstruct the continuous two-dimensional attenuation function. The problem however, is to solve (1.1) for $\mu(x,y)$ given data only for a finite number of projections [2]. This is accomplished by calculating $\mu(x,y)$ at a finite number of points, and involves the application of either iterative or analytical methods.

With iterative methods, the usual strategy is to divide the object into an array of pixels, and apply corrections to each cell coefficient such that the most recently calculated ray-projection matches the actual measured ray-projection. Several iterative techniques are concisely described in [3], including:

i) The Iterative Least-Squares Technique (ILST) which handles noisy data but often diverges due to over-correction. This approach has also been used for three-dimensional reconstruction by stacked two-dimensional reconstructions [4];

ii) The Simultaneous Iterative Reconstruction Technique (SIRT) which also accepts noisy data but executes very slowly because of the large number of mutiplications required; and

iii) The Algebraic Reconstruction Technique (ART) [5] which converges rapidly but is unable to operate on noisy data.

Also, as a general rule, most iterative procedures are sensitive to the sequence in which projections are chosen, preferring large angles between consecutive projections.

With analytical methods the solution of (1.1) is obtained directly using either Two-Dimensional Fourier Reconstruction or Convolution Filtered Back-Projection [6]. The band-limiting employed in these methods causes the elimination of spatial frequencies greater than a prespecified maximum,

thus limiting the resolution of the final image. For instance, depending on how sharp the cut-off filter is, boundary overshoot (the Gibbs phenomenon) may be observed. On the other hand an aliasing effect might occur if band-limiting is not used, especially near high frequency zones such as media boundaries. Both iterative and analytic methods employ filtering techniques as a means of suppressing either patient motion artifact or numerically introduced artifact. Filtering is particulary important for edge enhancement applications.

Another difficulty common to analytic methods is the interpolation required in the Fourier domain. Recalling that only one-dimensional projection data is available, it is clear that only corresponding one-dimensional Fourier transforms can be obtained. Yet, to generate an image, it is necessary to find the two-dimensional Fourier transform in order to acquire the sampling points needed by the inverse transform operation. This leads to a significant amount of interpolation in the Fourier domain, a task which could cause an excessive computational burden.

Whichever method is used, the projections must provide enough data so that there are as many equations as there are unknown attenuation function values. In other words, an appropriate set of independent measurements is essential.

Mathematically, the X-ray imaging problem can be reduced

to finding the solution of the linear system of equations

$$A\underline{d} = \underline{p} \tag{1.3}$$

where A is a coefficient matrix, $\underline{d}$ is a vector of unknown cell densities, and $\underline{p}$ is a vector of line integral measurements for each ray-projection [7]. If extra projections are available the image becomes overdetermined and reconstruction will yield an averaged image in which noise and interpolation error has been reduced. If too few projections are available the image becomes underdetermined and the reconstruction is inaccurate and laden with artifact.

Although large changes in density only occur at interfaces between bone and soft tissue or air, X-ray tomography has nevertheless been used to detect differences in soft tissue density as low as 0.5%. For example, it is now possible to distinguish between cerebrospinal fluid cavities and brain tissue, or even between white and grey matter. Unfortunately however, this order of resolution is not possible in every application. Often, as with lung disease, the most useful way to employ X-ray imaging is to increase the X-ray dosage and possibly over-expose certain organs. Radiation hazard is a significant drawback to X-ray reconstruction, as is scanner size and cost. Furthermore, X-ray methods are relatively slow and thus unable to follow the dynamic activity of body organs.

In summary, this section has presented the main concepts of transmission tomography and has indicated several of the method's problem areas. Much of the detail was included because of similarities present in other not so well-known imaging techniques. It is hoped this will assist in understanding the other methods, particularly Impedance Computed Tomography.

1.2 OTHER IMAGING TECHNIQUES

A relatively recent three-dimensional imaging technique [8] known as Positron Emission Tomography (PET) is based on the determination of the distribution of gamma-emitting radionuclides in the human body. The method measures changes in chemistry of injected radiopharmaceutical compounds by detecting released photons during radioactive decay. From these changes the emitted photon source location can be determined. A PET reconstruction represents the radionuclide concentration in the body at a given time after injection, and can be used to investigate brain and heart metabolism, detect cancer, or even determine myocardial infarction volume [9]. Again however, the scanning equipment is both large and expensive and the method itself has the undesireable requirement of injecting a radioactive substance into the human body.

Nuclear Magnetic Resonance (NMR) is another imaging technique which is also similar to X-ray tomography; but instead

of X-rays NMR employs Radio Frequency (RF) radiation in the presence of a magnetic field [10]. Broadband RF pulses excite tissue nuclei which then precess at a rate proportional to the magnetic field strength at that spatial location. By measuring the total magnetic energy as a function of frequency, the integrals of the spin density of hydrogen nuclei can be obtained. This procedure is analogous to finding an X-ray projection, and the inversion proceeds in a somewhat similar manner. A significant advantage of NMR is that it does not use ionizing radiation nor does it present a known hazard [11]. A major problem is that NMR equipment is very expensive and limited mostly to research applications.

Another reconstruction method involves the use of ultrasonics. Typically, short bursts of ultrasonic energy are directed through the image space and appropriate attenuation and delay time measurements are recorded. These measurements are used to generate absorbtion and velocity profiles (projections). The inversion is performed iteratively as in X-ray tomography, possibly with an additional allowance for ray curvature [12]. Currently, efforts are being directed towards substituting ultrasonic tomography for X-ray tomography where possible, even though there is evidence which indicates that ultrasonic energy absorbed by a living body is not entirely innocuous [49,50]. Another problem is that diaphonous objects (those with small variations in the acoustic refraction index) cannot be imaged very well. This

is particularly true in soft tissues such as the lung where ultrasound is highly attenuated.

Some of the other imaging methods discussed in the literature include;

a) Microwave imaging by the ART algorithm, which is potentially more sensitive and less hazardous than conventional X-Ray techniques [13];

b) Cardiopulmonary imaging, which is based on measuring the body surface field distribution resulting from high frequency electromagnetic stimulation. Thereafter, this technique incorporates a calculation of the apparent interior resistivity distribution [14]; and

c) Resistive imaging, for which background information is reviewed in the next chapter, followed by a presentation of new recovery algorithms.

Chapter II

REVIEW OF RESISTIVE IMAGING

Since neither X-ray nor ultrasonic imaging is adequate for every application, attention is gradually shifting to methods which rely on different physical properties of the media. For example, consider imaging an electrical parameter such as conductivity (or resistivity) from current injection data. This technique may be especially important in the medical area as weak electrical currents are believed to have no adverse effects on humans.

The remainder of this chapter provides information pertaining to the variation of electrical parameters in dielectric media; discusses nonimaging impedance-based techniques; and reviews several existing approaches to resistive tomography. Novel algorithms for resistive imaging are presented in following chapters.

2.1 MEDIA PROPERTIES

The two electrical properties of interest in impedance imaging are conductivity and permittivity. However, if excitation frequencies are low enough -- approximately on the order of 1 kHz. -- then for most media reactive effects are negligible [15] and the technique is referred to as resis-

tive imaging (or its reciprocal, conductivity imaging). The method relies heavily on the variation of resistivity magnitude throughout the region; slight resistivity changes would be much more difficult to image than order of magnitude variations.

Typical resistivity/conductivity values of human body tissue reported in the literature [16] are:

a) Blood @ 160 ohm-cm or 6.25 millimho/cm;

b) Lung @ 2000 ohm-cm or 0.50 millimho/cm;

c) Liver @ 700 ohm-cm or 1.40 millimho/cm; and

d) Heart muscle (anisotropic) @ 250 & 550 ohm-cm or 4.0 & 1.8 millimho/cm.

These estimates were obtained using a four probe measurement technique that eliminated the effect of contact resistance on the measurements. However, the reliability of such data is still questionable since much of the testing was done after death when cell membranes could no longer maintain proper ionic gradients. In this situation tissue resistivity may change within 30 to 60 minutes [17], thus affecting the measurements.

Observation of the above data leads to the conclusion that conductivity ratios for various body organs are as high as 12.5 to 1.0. This satisfies the previously discussed imaging criterion that resistivity variations be significant. Similar sets of conductivity data have been tabulated for a variety of soils and rocks [18] and again, the ratios vary

significantly from one region to the next. The implication is that resistive imaging may also apply to the important field of geophysical prospecting/subsurface exploration.

Considerable effort has been expended to study the effect of media inhomogeneities upon electrical fields, especially in medical applications. In one such study, three-dimensional finite element models were used to evaluate proposed techniques for recording thorax impedance during cardiovascular function monitoring [19]. Interior body tissue structures such as lungs, muscle walls, and ventricles were conveniently modelled and tested under boundary conditions appropriate to the particular impedance measurement technique being investigated.

In another study [20], two-dimensional finite element analysis was employed to analyze the sensitivity of body surface potentials to interior changes in conductivity. Various simulations indicated that even small conductivity changes -- such as an increase in lung water -- would cause significant surface potential changes, thereby improving the chance of detecting internal conductivity change by external measurements.

A third study applied finite difference methods to electric field calculations [21]. Successful models were established of intracranial fields due to brainstem dipole neural generators, and researchers were able to predict the effect of local brain inhomogeneities on the fields.

Taken together, these studies demonstrate that conductivity differences within a media can be detected and observed by external measurement procedures so long as these differences are relatively significant.

2.2 BIOPHYSICAL IMPEDANCE METHODS

The process of monitoring impedance fluctuations in the body to determine heart and lung changes is known as impedance plethysmography. An important development occurred in 1970 with the advent of an Impedance Cardiograph unit [22] for use in impedance plethysmography. By injecting a constant current through the thorax and measuring the potential difference between two electrode bands -- which were secured around the thorax but not connected to either injection electrode -- it was possible to obtain an estimate of the mean thorax impedance and the rate of change of this impedance during a cardiac cycle. These two parameters were then used to assess cardiac output, lung volume and intrathoracic fluid accumulation. Using such an approach, attempts have been made to explain the relationships between impedance waveforms and biomedical events. For example, some researchers have concluded that impedance cardiography yields very useful information about the haemodynamics of various body organs [23].

Isopotential mapping has also been employed in medical applications. A device was constructed for electrocardio-

graphic or electroencephalographic use [24], which took an array of voltage measurements over a body area and provided a simultaneous display of the collected data. However, the technology available at that time was just too slow to provide real time data collection and display capabilities. Other researchers later provided a high speed data acquisition and display unit [25] which could be updated after each cardiac cycle. They also utilized computer processing of the collected data to produce isopotential maps from 2,048 self-generated locations on the chest surface.

The impedance plethysmography method may be modified to include a set of pickup electrodes for body surface voltage measurements, in which case it is known as electric-field plethysmography [26]. This method allows the examination of surface electrode potential differences and yields information about heart position and cardiac output with very little interference from changes in lung conductivity.

The next major innovation, the Impedance Camera [27], represented a sort of hybrid of the above methods, and sought to display isoadmittance contours of the chest rather than isopotentials. A regular array of eighty mutually guarded electrodes was fixed to a patient's back, and a one volt signal was applied across the whole chest area. The guarding procedure was intended to effect a long and narrow measurement volume positioned on each electrode. Current flow through each electrode was recorded, and the corre-

sponding volume's impedance calculated and processed for contour display. This technique is very crude however, as the measurements do not really account for current spread throughout inhomogeneous body organs.

Note that although any of these biophysical impedance methods will allow for physiological interpretation of measured data, none of them can perform image reconstruction.

2.3 RESISTANCE PROJECTION METHODS

The main impediment to resistive reconstruction is the fact that electrical currents do not travel in straight lines, but rather they travel a path which is entirely object dependent. In resistive imaging the current path can only be determined from precise knowledge of the conductivity distribution, while conductivity reconstruction can only be accomplished with knowledge of the current flow paths. Algebraically this may be expressed as

$$A(d)\underline{d} = \underline{p} \qquad (2.1)$$

where the coefficient matrix A depends on the solution $\underline{d}$. The problem is therefore nonlinear and cannot be solved with the same algorithms used for (1.3) since the left-hand side cannot be accurately evaluated unless the current paths are known.

An extension to the previously discussed ART algorithm has been proposed [28] which attempts to handle such nonlinearities. The method is based on the solution of Laplace's equation -- under measured boundary conditions -- within an iterative loop. The physical arrangement consists of an object (inside a water tank) and a regular array of electrodes that are secured to the tank's outer surface. A measured projection is obtained by applying a known voltage to the electrode array, measuring the current flow through various electrodes, and calculating gross impedance values at each measurement site. The object inside the tank is then rotated, thereby altering the current flow paths as well as the measured current. The result is a set of resistance projections (or a profile) for each object angle.

To initiate the recovery process a conductivity distribution is assumed and the electric field numerically computed. After streamlines (or current paths) are determined from the potential field gradients, resistance projections along the current paths are calculated for each object orientation angle. Comparing calculated against measured resistance projections allows the original estimate of conductivity distribution to be corrected by a back-projection technique. Repetition of this procedure continually updates current flow paths and resulting conductivity estimates. Typically, only several iterations are required for the process to converge; however, this does not mean an accurate solution has been obtained.

Often, the mean-square reconstruction error can be as high as 30% when compared to the "exact" solution. In some cases convergence may not even be possible unless a mathematical operation such as smoothing or underrelaxation is performed between conductivity iterations. In other cases the number of different projection angles needed to obtain a reasonable image is excessive (e.g. greater than 400), thus increasing the required computational effort.

A similar approach using impedance projections and a modified ART algorithm [29], but with many more electrodes, has been proposed for certain moderate-resolution geophysical applications. The main objective is to develop an impedance camera useful for geophysical diagnostics in geological and mineral prospecting applications. In the past this was done with crude electrical impedance methods [30] which calculated an apparent subsurface resistivity of horizontally layered models [31]. Potential applications of the impedance camera are said to include core sample and borehole analysis, as well as general subsurface imaging.

Almost all proposed impedance computed tomography methods are based on the resistance projection techniques just described. Inherent to these techniques is the important assumption that current paths follow essentially straight lines, much the same as X-ray beams. In reality, current flow paths are highly object dependent and this assumption is fallacious, even when guard electrodes are employed. Be-

cause of this some researchers argue that it is not possible to perform impedance reconstruction by standard projection methods. Instead, they point out the need for alternative schemes and suggest an approach in which general distributions of conductivity may be reconstructed by a "modal" identification and measurement process [32].

The point to stress is that more information is needed for conductivity reconstruction than could easily be obtained from the usual resistance projection methods. The next two chapters outline a new procedure which may yield this additional information.

2.4 NETWORK FAULT DETECTION

Although the previous section emphasized imaging of continuous conductivity distributions, the problem of imaging (or discovering) discrete network parameters is also very important. This is especially true in view of the growing demand for automatic testing and fault analysis of computer systems. In either case the objective is to calculate circuit component values from sets of node point measurements and determine those components which do not meet a specific tolerance criterion. If detection of unacceptable components could be done automatically this would certainly alleviate a significant amount of the cost burden associated with manual search and detect methods.

It is possible to employ Tellegen's theorem to establish a relationship between current and voltage changes in an original circuit and an adjoint circuit. Under suitable branch constraints this method may uniquely determine component variations from limited sets of port measurements. However, to accomplish this it is very important to obtain enough independent port measurements to solve all unknown component values. Other techniques have been used for detection of multiple faults in analog circuits [33]. Another algorithm [34] employs graph theory and suggests necessary and sufficient conditions for discovering particular network components. Other techniques, more general in scope, attempt to direct current in a beam-like fashion through the resistor mesh [35] and acquire sets of profile measurements for processing in a manner similar to X-ray computed tomography. Because these techniques have only been partially successful, discrete network imaging remains an unsolved problem.

The next chapter presents a novel algorithm for determining resistive network component values from limited sets of measurements.

Chapter III

IMAGING RESISTANCE NETWORKS

The network imaging algorithm presented in this chapter effectively decouples the nonlinear system described by (2.1) into three linear subsystems which are subsequently iterated until convergence is achieved. Two of the linear subsystems are used for determining node potentials while the third is used for calculating branch conductances. The node potential formulation will be considered first, followed by a presentation of the branch conductance calculation and the network imaging algorithm.

3.1 DETERMINING NODE POTENTIALS

Consider the resistor mesh of Fig. 3.1. Application of Kirchoff's Current Law to an independent set of network nodes leads to the linear system of equations

$$Y\tilde{\underline{v}} = \underline{j} \tag{3.1}$$

where Y is the nodal admittance matrix, $\tilde{\underline{v}}$ is the vector of unknown node potentials and $\underline{j}$ is the source vector. Here, the node potentials result from imposition of currents at selected boundary points.

If voltages were imposed instead of currents, a different set of node potentials would result. This alternative is expressed as

$$Y\underline{v} = \underline{0} \qquad (3.2)$$

where Y is the same nodal admittance matrix, but $\underline{v}$ consists of both known and unknown node potentials.

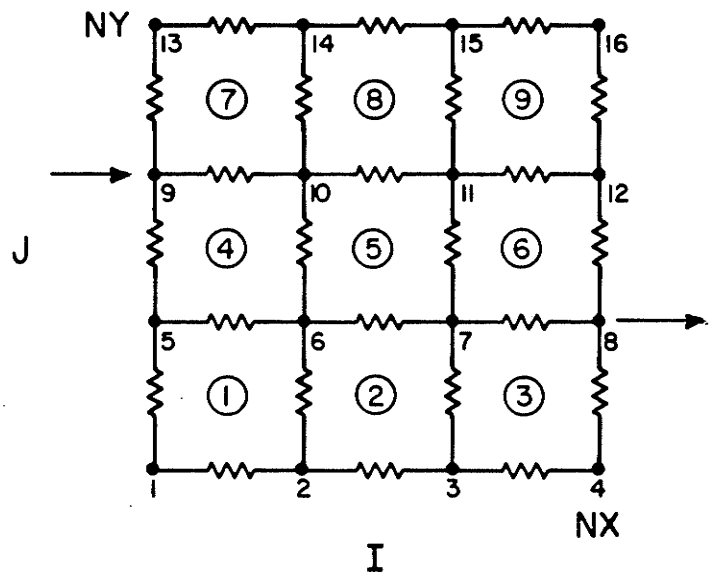

Figure 3.1: Resistor Network.

The problem is to solve (3.1) and (3.2) for the unknown potentials. It is usual to assign at least one node as a reference point, and then to perform row eliminations and column transfers to the right-hand side, thus eliminating the admittance matrix singularity. Fortunately, for imaging purposes this is not necessary.

Even though the admittance matrix is singular, both systems can be solved using either a point-iterative or a pre-conditioned conjugate gradient method. However, with this approach the solution will only be correct to within an arbitrary constant [36]. Later it will be shown that the arbitrary constant is irrelevant since the imaging algorithm ultimately requires only potential gradient information.

The Nodal Admittance Matrix

Construction of the nodal admittance matrix is a relatively straightforward procedure. Fig. 3.1 illustrates typical numbering schemes for mesh nodes and mesh loops. For ease of programming it is best to cycle through all loops and perform a random accumulation of admittance matrix entries for every node contained within each loop.

As each loop is selected -- and depending upon the location of the loop in the mesh -- it is necessary to choose from one of the four possible accumulation patterns depicted in Fig.'s 3.2 - 3.5. After processing all loops the admittance matrix has been completely assembled, and equations (3.1) and (3.2) are easily solved for the unknown potentials.

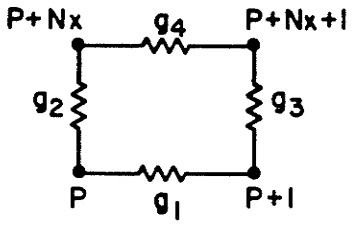

$$Y_{P,P} \leftarrow g_1 + g_2$$

$$Y_{P+1,P+1} \leftarrow g_1 + g_3$$

$$Y_{P+Nx,P+Nx} \leftarrow g_2 + g_4$$

$$Y_{P+Nx+1,P+Nx+1} \leftarrow g_3 + g_4$$

$$Y_{P,P+1} \leftarrow -g_1$$

$$Y_{P,P+Nx} \leftarrow -g_2$$

$$Y_{P+1,P+Nx+1} \leftarrow -g_3$$

$$Y_{P+Nx,P+Nx+1} \leftarrow -g_4$$

Figure 3.2: Accumulation for Top Right Corner Loop.
I=NX-1 J=NY-1 P=I+(J-1)NX

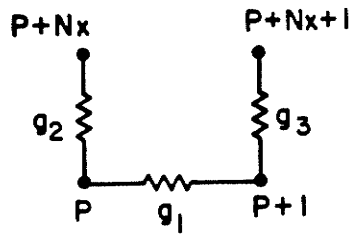

$$Y_{P,P} \leftarrow g_1 + g_2$$

$$Y_{P+1,P+1} \leftarrow g_1 + g_3$$

$$Y_{P+Nx,P+Nx} \leftarrow g_2$$

$$Y_{P+Nx+1,P+Nx+1} \leftarrow g_3$$

$$Y_{P,P+1} \leftarrow -g_1$$

$$Y_{P,P+Nx} \leftarrow -g_2$$

$$Y_{P+1,P+Nx+1} \leftarrow -g_3$$

Figure 3.3: Accumulation for Right Side Loops.
I=NX-1 J=1..(NY-1) P=I+(J-1)NX

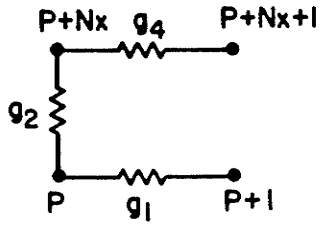

$$Y_{P,P} \leftarrow g_1 + g_2$$

$$Y_{P+1,P+1} \leftarrow g_1$$

$$Y_{P+Nx,P+Nx} \leftarrow g_2 + g_4$$

$$Y_{P+Nx+1,P+Nx+1} \leftarrow g_4$$

$$Y_{P,P+1} \leftarrow -g_1$$

$$Y_{P,P+Nx} \leftarrow -g_2$$

$$Y_{P+Nx,P+Nx+1} \leftarrow -g_4$$

Figure 3.4: Accumulation for Top Side Loops.
I=1..(NX-1) J=NY-1 P=I+(J-1)NX

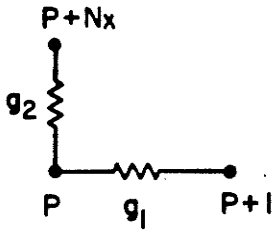

$$Y_{P,P} \leftarrow g_1 + g_2$$

$$Y_{P+1,P+1} \leftarrow g_1$$

$$Y_{P+Nx,P+Nx} \leftarrow g_2$$

$$Y_{P,P+1} \leftarrow -g_1$$

$$Y_{P,P+Nx} \leftarrow -g_2$$

Figure 3.5: Accumulation for All Other Loops.
I=1..(NX-2) J=1..(NY-2) P=I+(J-1)NX

Node Potentials Due To An Applied Current

Using the pre-conditioned conjugate gradient method to solve (3.1), for an impressed current input and withdrawal of one amp, yields the node potentials of Fig. 3.6. The conductivity network employed by this calculation is also given in the same figure.

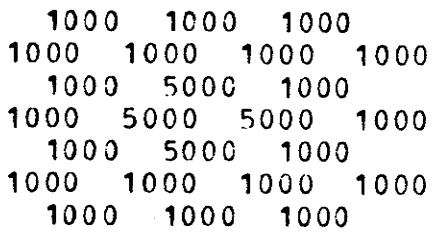

Conductivity Mesh

0.034	-0.077	-0.300	-0.800
0.145	0.034	-0.022	-0.300
0.367	0.089	0.034	-0.077
0.867	0.367	0.145	0.034

Node Potentials

Figure 3.6: Node Potentials for Impressed Current.

Node Potentials Due To An Applied Voltage

The same network, but with voltages impressed at all boundary nodes rather than current at two nodes, results in the node potentials of Fig. 3.7. When solving a singular matrix the solution only will be correct within an arbitrary constant (we are only concerned with gradients so the constant is not relevant). For example, in the figure below we find the same boundary potentials as in the previous figure by subtracting the constant 0.008 from all nodes.

```
      1000   1000   1000
1000   1000   1000   1000   1000
      1000   500C   1000
1000   5000   5000   1000
      1000   500C   1000
1000   1000   1000   1000
      1000   1000   1000
```

0.833	0.722	0.500	C.000
0.944	0.833	0.778	0.500
1.167	0.889	0.833	0.722
1.667	1.167	0.944	C.833

Figure 3.7: Node Potentials for Impressed Voltage.

3.2 CALCULATING BRANCH CONDUCTANCES

Once the potentials have been obtained at all network nodes, the branch conductivities may be determined. Consider Ohm's law as it applies to a single-conductor branch

$$gv = j \qquad (3.3)$$

where g is the branch conductivity, v is the branch voltage, and j is the branch current. If a branch is considered to extend from node i to node j then (3.3) may also be expressed as

$$g_{ij}(v_i - v_j) = j_{ij} \tag{3.4}$$

where g_{ij} represents branch conductance and j_{ij} is branch current, but v_i and v_j are node voltages.

The Least-Squares Residual

Treating branch conductances as unknowns and considering all excitations, x, allows the formation of a least-squares residual from (3.4)

$$r = \sum_x \sum_{b_{ij}} \{(v_i - v_j)g_{ij} - j_{ij}\}^2 \tag{3.5}$$

which can be minimized by taking the partial derivative with respect to branch conductance and equating it to zero

$$\frac{\partial r}{\partial g_{ij}}\bigg|_{b_{ij}} = \sum_x 2\{(v_i - v_j)g_{ij} - j_{ij}\}(v_i - v_j) = 0 \tag{3.6}$$

Conductance Equations in Point Form

Simplifying (3.6) gives

$$\sum_x (v_i - v_j)^2 g_{ij} = \sum_x j_{ij}(v_i - v_j) \qquad (3.7)$$

and solving for the unknown branch conductance yields

$$g_{ij} = \frac{\sum_x j_{ij}(v_i - v_j)}{\sum_x (v_i - v_j)^2} . \qquad (3.8)$$

The branch currents are not known in advance and must be determined prior to employing (3.8) in a conductance calculation. Typically, they are obtained from (3.1), in which case (3.8) becomes

$$g_{ij} = \frac{\sum_x (\tilde{v}_i - \tilde{v}_j)\tilde{g}_{ij}(v_i - v_j)}{\sum_x (v_i - v_j)^2} \qquad (3.9)$$

where v_i and v_j are derived from an assumed set of network conductance values, $\tilde{g}_{ij}$, under an applied boundary voltage, while $\tilde{v}_i$ and $\tilde{v}_j$ are based on the same network under an applied boundary current.

Conductance Solution From Exact Potentials

If the exact potentials are known, say from measurements on the network, but the conductance values are unknown, then it is possible to iterate through (3.9) and improve the original g_{ij} estimate. The procedure is repeated until convergence is achieved, at which time the best fit (in a least-squares sense) conductance network will have been attained.

Fig. 3.8(a) shows an "exact" network from which node potentials are obtained for both an applied voltage and an applied current. These computer simulated measurements were used in (3.9) along with the initial conductivity assumption of Fig. 3.8(b). The final result after thirty iterations is depicted in Fig. 3.8(c).

```
      1000   1000   1000
1000   1000   1000   1000   1000
      1000   5000   1000
1000   5000   5000   1000
      1000   5000   1000
1000   1000   1000   1000
      1000   1000   1000
```

(a)

```
      1000   1000   1000
1000   1000   1000   1000
      1000   1000   1000
1000   1000   1000   1000
      1000   1000   1000
1000   1000   1000   1000
      1000   1000   1000
```

(b)

```
      1000   1001   1000
1000    999   1001   1000
      1000   4999   1000
1000   4996   5005   1000
      1000   4999   1000
1000    999   1001   1000
      1000   1001   1000
```

(c)

Figure 3.8: Network Conductor Values.

3.3 THE NETWORK IMAGING PROCESS

When neither branch conductances nor node potentials are known, one must resort to a hybrid algorithm employing both of the previously discussed methods of finding node potentials in conjunction with the technique for determining branch conductances. During the imaging process it is the boundary potential information which connects the three linearized subprocesses together thus leading to successful network recovery.

In Fig. 3.9(a) an "exact" network is modelled. Using boundary excitations, the node potentials are determined at all boundary nodes for each independent excitation. In practice the boundary potentials are measured rather than simulated by a computer program.

The solution process is initiated by providing a guess of all network conductor values (usually all set to the same value) and then generating the two sets of node potentials indicated by Fig. 3.9(b) and Fig. 3.9(c). The node potentials of Fig. 3.9(b) are obtained for the same current excitations used in Fig. 3.9(a), while the potentials of Fig. 3.9(c) are derived from enforced boundary voltages.

Fig. 3.9(d) shows that the next conductance estimate is generated from a combination of: the most recent conductance estimate; the node potentials of Fig. 3.9(b) which result from applied currents; and the node potentials of Fig. 3.9(c) which are due to applied boundary voltages.

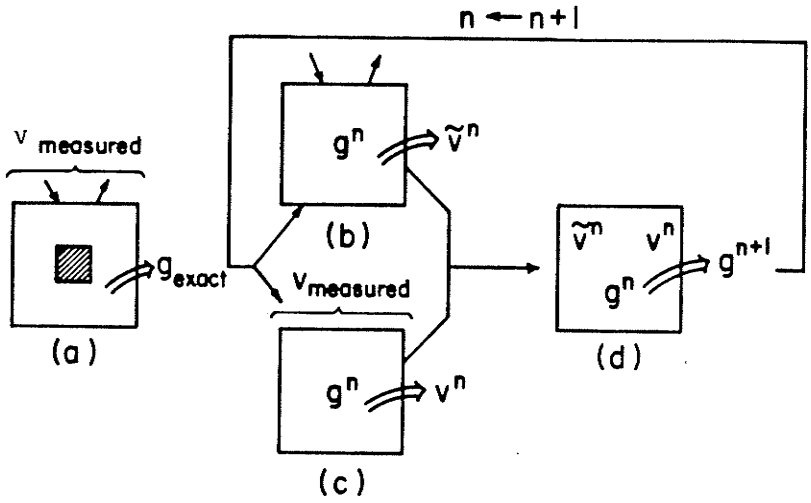

Figure 3.9: Network Imaging Process.

3.4 NETWORK RECONSTRUCTION SIMULATIONS

A number of examples follow which illustrate both the success this algorithm has achieved thus far, and the difficulties which have yet to be overcome. In all cases the original network appears on the left-hand side of the figure while the recovered version is located on the right-hand side.

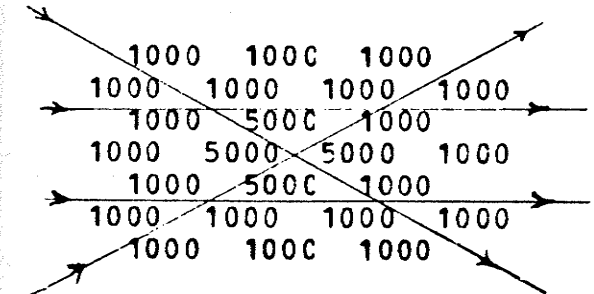

Exact solution and four excitation pattern used in all simulations.

1000 1004 1001 1000 997 1005 999 1003 4843 1004 998 5140 4850 1000 1003 4844 1004 1000 997 1005 999 1000 1004 1001	500 Iter.
1000 1000 1000 1000 1000 1000 1000 1000 4999 1000 1000 5000 5000 1000 1000 4999 1000 1000 1000 1000 1000 1000 1000 1000	2000 Iter.

Figure 3.10: One High Conductance Patch.

```
                                    5000   987   999
                                 5000  5064  1009  1001
                                   4960  1031  4724
                                1013   956  4664  5107     400
                                   978  1035  4750         Iter.
                                1000  1020   999  1002
                                  1000   987   998
  5000  1000  1000
5000  5000  1000  1000
  5000  1000  5000
1000  1000  5000  5000
  1000  1000  5000
1000  1000  1000  1000
  1000  1000  1000
                                   5000   999  1000
                                5000  5005  1000  1000
                                  4998  1002  4986
                                1001   996  4989  5004     1000
                                   999  1001  4989         Iter.
                                1000  1001  1000  1000
                                  1000   999  1000
```

Figure 3.11: Two High Conductance Patches.

```
                                   1000   998  1000
                                1000  1001   998  1000
                                   998  1016   998
                                1000   999  1003   999     800
                                  1003  4855  1004         Iter.
                                1000   998  1002  1000
                                  1000  1004  1000
  1000  1000  1000
1000  1000  1000  1000
  1000  1000  1000
1000  1000  1000  1000
  1000  5000  1000
1000  1000  1000  1000
  1000  1000  1000
                                  1000  1000  1000
                               1000  1000  1000  1000
                                  1000  1000  1000
                               1000  1000  1000  1000     1600
                                  1000  4999  1000         Iter.
                               1000  1000  1000  1000
                                  1000  1000  1000
```

Figure 3.12: A Single Resistor.

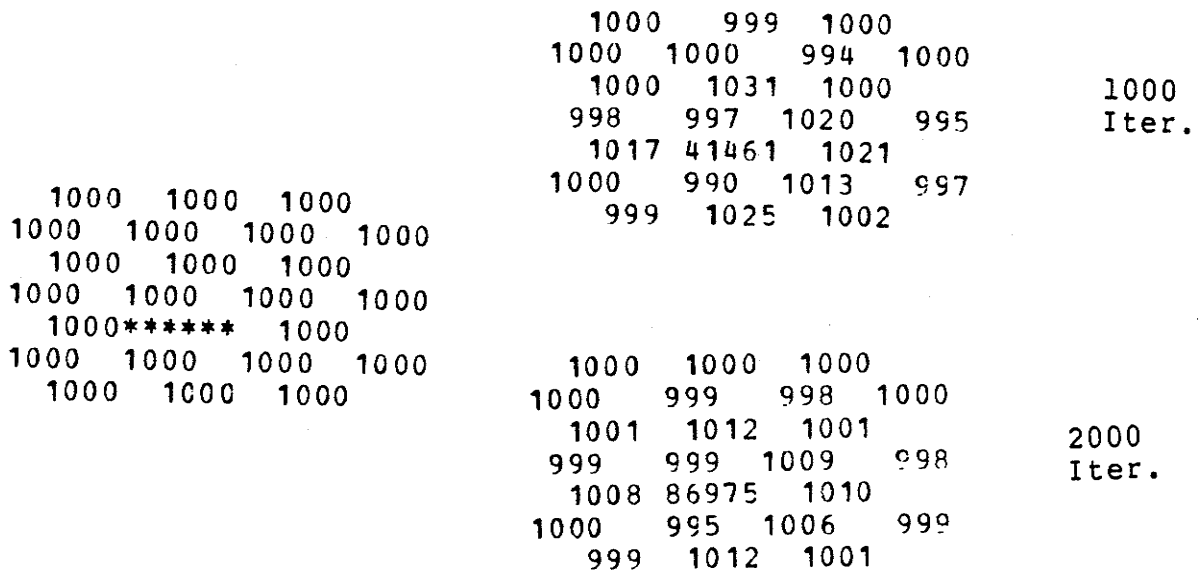

Figure 3.13: Short Circuit Fault Detection.

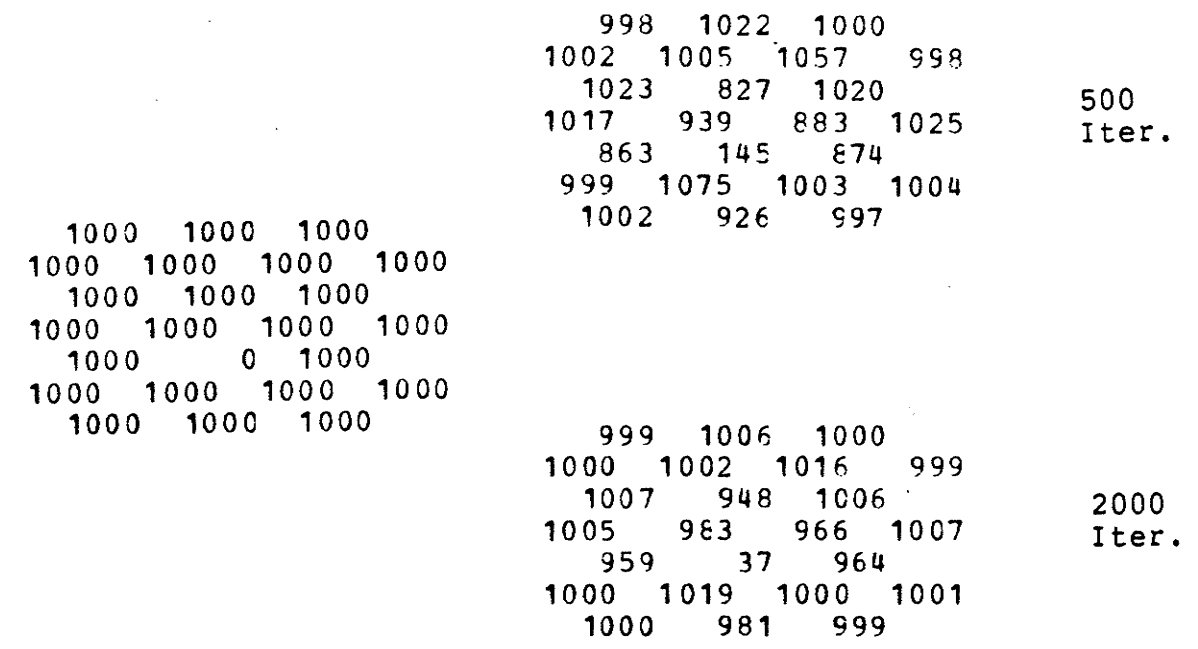

Figure 3.14: Open Circuit Fault Detection.

Chapter IV

FINITE ELEMENT RESISTIVITY INVERSION

This chapter considers the problem of reconstructing both two and three-dimensional distributions of electrical conductivity from boundary or surface potential measurements. The reconstruction process involves the solution of a nonlinear system of equations generated by finite element discretization, and obtains the best conductivity distribution -- in a least-squares sense -- from simulated data.

Analogous to the resistor network formulation, the method used here decouples the nonlinear system into three linear subsystems which are then solved simultaneously. Two of these subsystems are employed for solving the scalar electrostatic field while the other determines the conductivity distribution. The electrostatic field solution will be presented first.

4.1 ELECTROSTATIC FIELD SOLUTION

Assuming a given conductivity distribution, the required energy functional for solving Laplace's equation is

$$F = \int_V \kappa \nabla\phi \cdot \nabla\phi dv - 2\int_V \phi f dv \qquad (4.1)$$

which is valid for Dirichlet or homogeneous Neumann boundary conditions. Using the Rayleigh-Ritz discretization procedure

$$\phi = \underline{\phi}^T \underline{\alpha} = \underline{\alpha}^T \underline{\phi} \tag{4.2}$$

equation (4.1) becomes

$$F = \underline{\phi}^T \int_v \kappa \nabla \underline{\alpha} \cdot \nabla \underline{\alpha}^T dv \underline{\phi} - 2\underline{\phi}^T \int \underline{\alpha} f dv \ . \tag{4.3}$$

Differentiating with respect to the field unknowns yields

$$\frac{\partial F}{\partial \underline{\phi}} = 2\int_v \kappa \nabla \underline{\alpha} \cdot \nabla \underline{\alpha}^T dv \underline{\phi} - 2\int_v \underline{\alpha} f dv \tag{4.4}$$

which if equated to zero and rearranged becomes

$$\int_v \kappa \nabla \underline{\alpha} \cdot \nabla \underline{\alpha}^T dv \underline{\phi} = \int_v \underline{\alpha} f dv \tag{4.5}$$

(compare 4.5 against 3.1 and 3.2) or

$$S\underline{\phi} = \underline{b} \tag{4.6}$$

where

$$S_{ij} = \int_v \kappa_i \nabla\alpha_i \cdot \nabla\alpha_j dv \qquad (4.7)$$

and

$$b_i = \int_v \alpha_i f_i \, dv \; . \qquad (4.8)$$

Equation (4.6) is a system of linear equations that can be solved for the discretized field. One approach is to invoke a conjugate gradient procedure which accepts the S matrix and returns the calculated field values. Such routines have been developed by Nakonechny [47,48] at the University of Manitoba, and preliminary versions have been borrowed for use here. Another approach employs the point-iterative methods outlined in the Appendix. The next section shows how the point-iterative method could be used to obtain the discretized electric field solution.

Electric Field Equations In Point Form

Expanding along row i and solving for the i'th unknown gives

$$\phi_i = \frac{\int_v \alpha_i f dv - \sum_{j,j\neq i} [\int_v \kappa \nabla\alpha_i \cdot \nabla\alpha_j dv]\phi_j}{\int_v \kappa(\nabla\alpha_i \cdot \nabla\alpha_i)dv} \; . \qquad (4.9)$$

For ease of programming the conductivity and source may also be expressed as

$$\kappa = \underline{\alpha}^T \underline{\kappa} = \underline{\kappa}^T \underline{\alpha}$$
$$f = \underline{\alpha}^T \underline{f} = \underline{f}^T \underline{\alpha} \qquad (4.10)$$

so that (4.9) is now

$$\phi_i = \frac{\sum_j \int_v \alpha_i \alpha_j dv \, f_j - \sum_{j,j=i} [\sum_k \int_v (\nabla\alpha_i \cdot \nabla\alpha_j)\alpha_k \, dv \, \kappa_k]\phi_j}{\sum_k \int_v (\nabla\alpha_i \cdot \nabla\alpha_i)\alpha_k \, dv \, \kappa_k} \qquad (4.11)$$

As the shape functions are known, the required integrals are precalculated into equivalent weighting factor arrays. Thus (4.11) is simplified to

$$\phi_i = \frac{\sum_j V_{ij} f_j - \sum_{j,j\neq i} [\sum_k W_{ijk} \kappa_k]\phi_j}{\sum_\kappa W_{iik} \kappa_k} \, . \qquad (4.12)$$

If the conductivity is defined as constant throughout each element then (4.12) reduces to

$$\phi_i = \frac{\sum_j V_{ij} f_j - \kappa_i \sum_{j,j\neq i} W_{ij}\, \phi_j}{\kappa_i\, W_{ii}} \qquad (4.13)$$

resulting in a slight loss of modelling accuracy, but a modest improvement in programming effort and program execution time.

Current injection sites are easily handled by assigning f_i the numerical value of the impressed current density at the i'th node. Nodes which are to be held at a fixed potential are merely skipped over by the algorithm during the processing of (4.12) or (4.13).

Neumann Field Calculation

Imposing a current input and withdrawal of one amp on the conductivity distribution shown on the left-hand side of Fig. 4.1 results in the Neumann field pictured on the right-hand side.

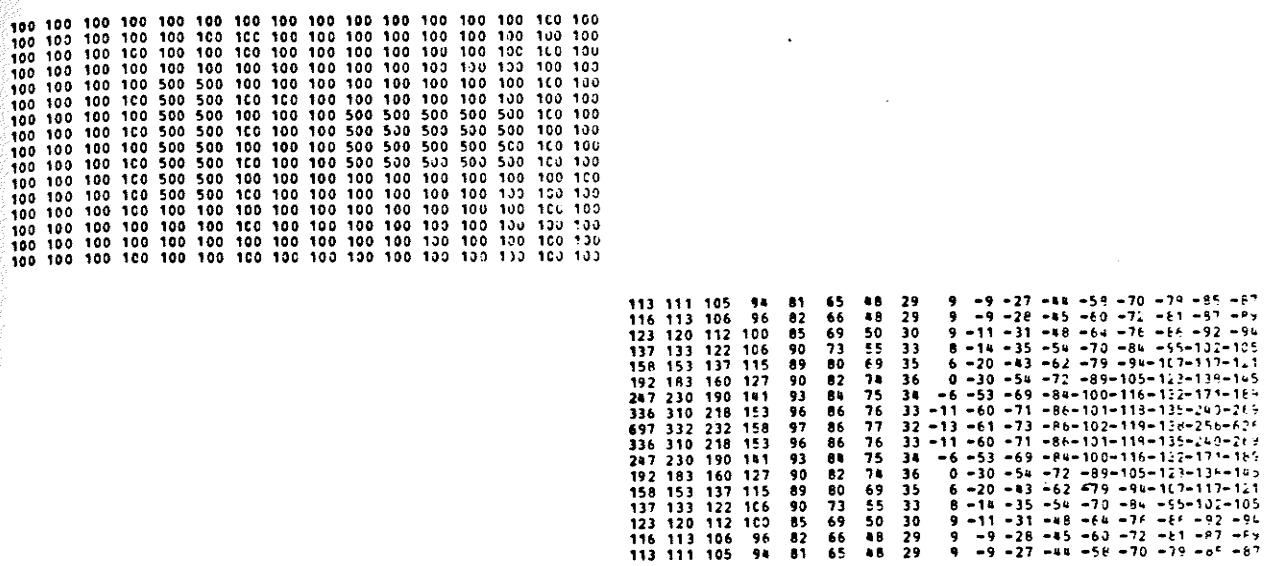

Figure 4.1: Conductivity Distribution and Neumann Field.

Dirichlet Field Calculation

The same conductivity distribution, but under an enforced boundary potential distribution results in the Dirichlet field of Fig. 4.2.

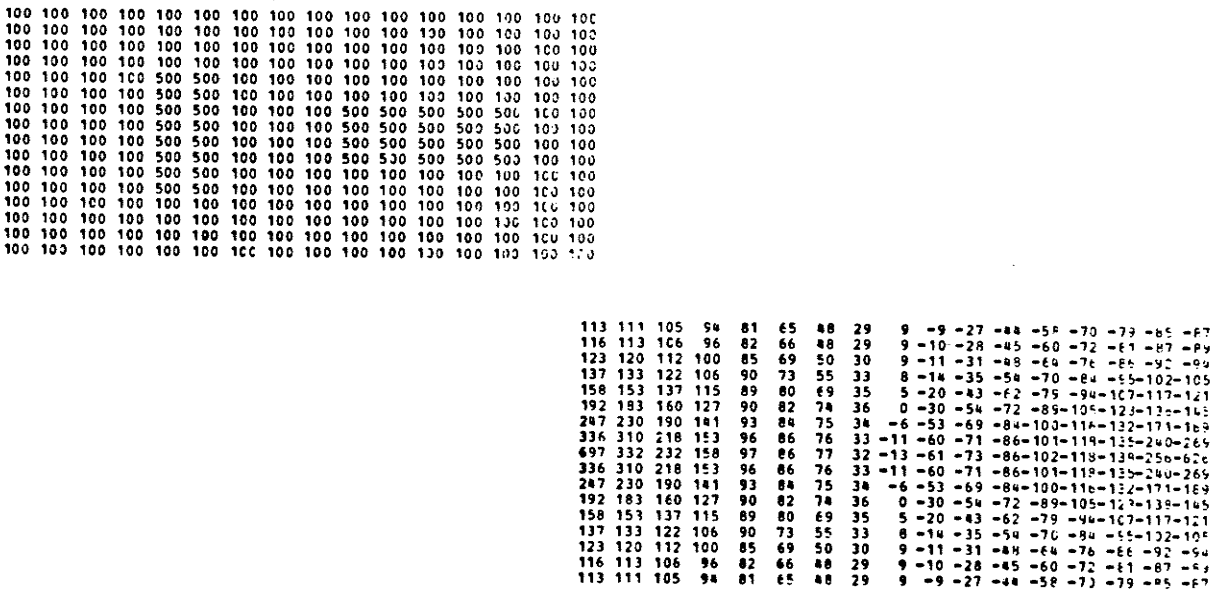

Figure 4.2: Conductivity Distribution and Dirichlet Field.

4.2 CONDUCTIVITY DISTRIBUTION SOLUTION

Once the potential field has been obtained throughout the region the conductivity distribution may be determined. Development of the spatial conductivity recovery method is based on the point form of Ohm's law, and closely parallels the branch conductance imaging technique of Chapter III.

The Least-Squares Residual

Recalling that

$$\bar{E} = - \nabla\phi \tag{4.14}$$

and

$$\bar{J} = \kappa\bar{E} = - \kappa\nabla\phi \tag{4.15}$$

(compare 4.15 to 3.3) a least-squares residual is formed

$$r = \sum_x \int_v (\kappa\nabla\phi + \bar{J})\cdot(\kappa\nabla\phi + \bar{J})dv \tag{4.16}$$

where x refers to current excitations. Taking the inner product

$$r = \sum_x \int_v ((\kappa\nabla\phi\cdot\nabla\phi\kappa) + \kappa\nabla\phi\cdot\bar{J} + \bar{J}\cdot\kappa\nabla\phi + \bar{J}\cdot\bar{J})dv \tag{4.17}$$

and simplifying produces

$$r = \sum_x \int_v (\kappa \nabla\phi \cdot \nabla\phi \kappa + 2\kappa \nabla\phi \cdot \bar{J} + \bar{J} \cdot \bar{J}) dv \ . \tag{4.18}$$

Substituting (4.10) into (4.18) gives

$$r = \sum_x \int_v (\underline{\kappa}^T \underline{\alpha} \nabla\phi \cdot \nabla\phi \underline{\alpha}^T \kappa + 2\underline{\kappa}^T \underline{\alpha} \bar{J} \cdot \nabla\phi + \bar{J} \cdot \bar{J}) dv \ . \tag{4.19}$$

As in (4.4), equation (4.19) may be minimized

$$\frac{dr}{d\underline{\kappa}} = 2\sum_x \int_v \underline{\alpha} \nabla\phi \cdot \nabla\phi \underline{\alpha}^T \cdot dv \underline{\kappa} + 2\sum_x \int_v \underline{\alpha} \bar{J} \cdot \nabla\phi dv = \underline{0} \tag{4.20}$$

and simplified to

$$\sum_x \int_v \underline{\alpha} \nabla\phi \cdot \nabla\phi \underline{\alpha}^T dv \underline{\kappa} = - \sum_x \int_v \underline{\alpha} \bar{J} \cdot \nabla\phi dv \tag{4.21}$$

which again represents a linear system.

Conductivity Equations In Point Form

Solving (4.21) for the conductivity at the i'th node produces (compare 4.22 to 3.8)

$$\kappa_i = \frac{\sum_x \int_v \alpha_i \bar{J}\cdot\nabla\phi dv - \sum_x \sum_{j,j\neq i} \int_v (\alpha_i \nabla\phi)\cdot(\nabla\phi\alpha_j) dv\, \kappa_j}{\sum_x \int_v (\alpha_i \nabla\phi)\cdot(\alpha_i \nabla\phi) dv} \quad . \tag{4.22}$$

Using (4.2) the x-component of the field gradient becomes

$$\frac{\partial\phi}{\partial x} = \frac{\partial \underline{\alpha}^T}{\partial x}\,\underline{\phi} = \underline{\phi}^T \frac{\partial \underline{\alpha}}{\partial x} = \sum_m \frac{\partial \alpha_m}{\partial x}\,\phi_m \quad . \tag{4.23}$$

The y and z-components are generated in a similar manner, thus (4.22) is now written as

$$\kappa_i = \frac{-\sum_x [\sum_m \int_v \alpha_i (J_x \frac{\partial\alpha_m}{\partial x} + J_y \frac{\partial\alpha_m}{\partial y} + J_z \frac{\partial\alpha_m}{\partial z}) dv\phi_m] - \sum_x \sum_{j,j\neq i} [\sum_\ell \sum_m \int_v \alpha_i\alpha_j (\frac{\partial\alpha_\ell}{\partial x}\frac{\partial\alpha_m}{\partial x} + \frac{\partial\alpha_\ell}{\partial y}\frac{\partial\alpha_m}{\partial y} + \frac{\partial\alpha_\ell}{\partial z}\frac{\partial\alpha_m}{\partial z}) dv\phi_\ell\phi_m]\kappa_j}{\sum_x [\sum_\ell \sum_m \int_v \alpha_i^2 (\frac{\partial\alpha_\ell}{\partial x}\frac{\partial\alpha_m}{\partial x} + \frac{\partial\alpha_\ell}{\partial y}\frac{\partial\alpha_m}{\partial y} + \frac{\partial\alpha_\ell}{\partial z}\frac{\partial\alpha_m}{\partial z}) dv\phi_\ell\phi_m]} \tag{4.24}$$

Since the current density is not known in advance it must be determined prior to employing (4.24) in a conductivity calculation. Initially, a conductivity distribution is assumed and using (4.2) the x-component of the current density can be expanded as

$$J_x = -\kappa \frac{\partial\tilde{\phi}}{\partial x} = -\sum_j \alpha_j \frac{\partial\tilde{\phi}}{\partial x}\kappa_j = -\sum_j \sum_\ell \alpha_j \frac{\partial\alpha_\ell}{\partial x}\tilde{\phi}_\ell\,\kappa_j \quad . \tag{4.25}$$

Performing similar expansions for J_y and J_z allows (4.24) to be written as

$$\kappa_i^{n+1} = \frac{\sum_x \{\sum_j [\sum_{\ell m} \int_v \alpha_i \alpha_j \left(\frac{\partial \alpha_\ell}{\partial x}\frac{\partial \alpha_m}{\partial x} + \frac{\partial \alpha_\ell}{\partial y}\frac{\partial \alpha_m}{\partial y} + \frac{\partial \alpha_\ell}{\partial z}\frac{\partial \alpha_m}{\partial z}\right) dv \tilde{\phi}_\ell \phi_m] \kappa_j^n - \sum_{j,j\neq i} \sum_{\ell m} \int_v \alpha_i \alpha_j \left(\frac{\partial \alpha_\ell}{\partial x}\frac{\partial \alpha_m}{\partial x} + \frac{\partial \alpha_\ell}{\partial y}\frac{\partial \alpha_m}{\partial y} + \frac{\partial \alpha_\ell}{\partial z}\frac{\partial \alpha_m}{\partial z}\right) dv \phi_\ell \phi_m \kappa_j^{n+1}\}}{\sum_x \{\sum_{\ell m} \int_v \alpha_i^2 \left(\frac{\partial \alpha_\ell}{\partial x}\frac{\partial \alpha_m}{\partial x} + \frac{\partial \alpha_\ell}{\partial y}\frac{\partial \alpha_m}{\partial y} + \frac{\partial \alpha_\ell}{\partial z}\frac{\partial \alpha_m}{\partial z}\right) dv \phi_\ell \phi_m\}} \qquad (4.26)$$

which, through the use of weighting factors, simplifies to

$$\kappa_i^{n+1} = \frac{\sum_x \{\sum_j [\sum_\ell \sum_m W_{ij\ell m} \tilde{\phi}_\ell \phi_m] \kappa_j^n - \sum_{j,j\neq i} \sum_\ell \sum_m W_{ij\ m} \phi_\ell \phi_m \kappa_j^{n+1}\}}{\sum_x \sum_\ell \sum_m W_{ii\ell m} \phi_\ell \phi_m} \quad . \qquad (4.27)$$

Again, further simplification is possible by employing constant valued conductivity elements. In this case (4.21) signifies a pure diagonal form and (4.27) reduces to

$$\kappa_i^{n+1} = \frac{-\kappa_i^n \sum_x \sum_\ell \sum_m W_{\ell m} \tilde{\phi}_\ell \phi_m}{\sum_x \sum_\ell \sum_m W_{\ell m} \phi_\ell \phi_m} \quad . \qquad (4.28)$$

The $\tilde{\phi}$ represents a field derived using natural Neumann boundaries while ϕ is derived from either total Dirichlet boundaries or from a combination of Neumann and Dirichlet boundary conditions.

Conductivity Solution From The Exact Field

If the exact potential fields are known, but the conductivity distribution is unknown, then it is possible to iterate through (4.27) or (4.28) and improve the original conductivity estimate. The procedure is repeated until convergence is achieved, at which time the best fit (in a least-squares sense) conductivity distribution will have been attained.

Fig. 4.3 shows an "exact" conductivity distribution from which the the electric field is obtained for both Neumann and Dirichlet boundary conditions. These computer simulated measurements were used in (4.28) along with the initial conductivity assumption which appears in the same figure. The final recovery after several iterations is also depicted.

Figure 4.3: Exact, Initial, and Recovered Conductivity Distribution.

4.3 THE IMAGING ALGORITHM

When neither the conductivity nor field distribution is known, one must resort to a hybrid algorithm employing the methods outlined in the previous sections. It is the boundary information -- either measured or simulated -- which connects the three linearized subprocesses together thus leading to successful image recovery.

In Fig. 4.4(a) an exact conductivity distribution is modelled. Using boundary excitations in two-dimensional problems and surface excitations in three-dimensional problems, the field distribution is determined for each independent excitation. In practice boundary or surface potentials would be measured rather than simulated.

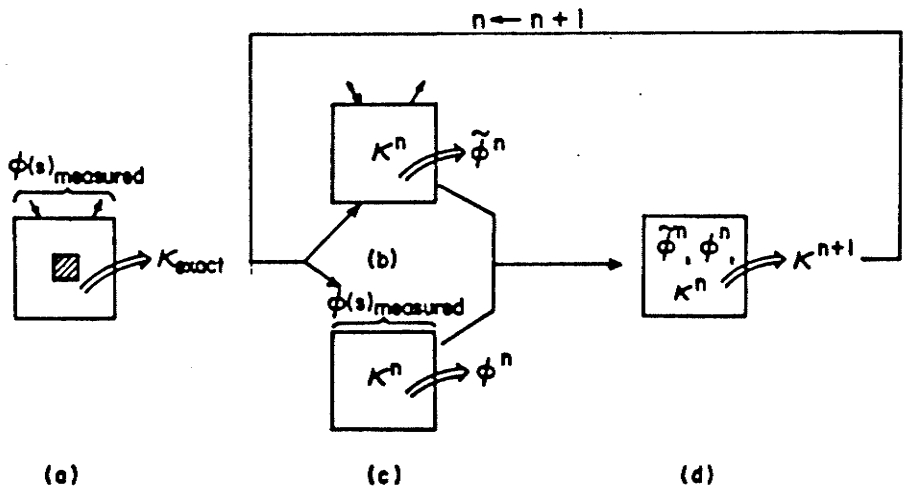

Figure 4.4: The Finite Element Imaging Process.

The solution process is initiated by estimating the conductivity distribution (usually homogeneous) and generating the two fields indicated by Fig.'s 4.4(b) and 4.4(c). The field of Fig. 4.4(b)is obtained -- with the same current excitations used in Fig. 4.4(a) -- under natural Neumann boundary conditions. The field of Fig. 4.4(c) is determined under Dirichlet boundary conditions. No currents are impressed during this phase of the calculation.

Fig. 4.4(d) shows that the next conductivity estimate is generated from a combination of:

i) the most recent conductivity estimate;

ii) the current density approximation (4.25) obtained via the Neumann field of Fig. 4.4(b); and

iii) the Dirichlet field of Fig. 4.4(c).

This process is repeated until the desired accuracy is achieved.

Fig. 4.5 presents a flowchart in which the conjugate gradient method is used to obtain the electric field estimate.

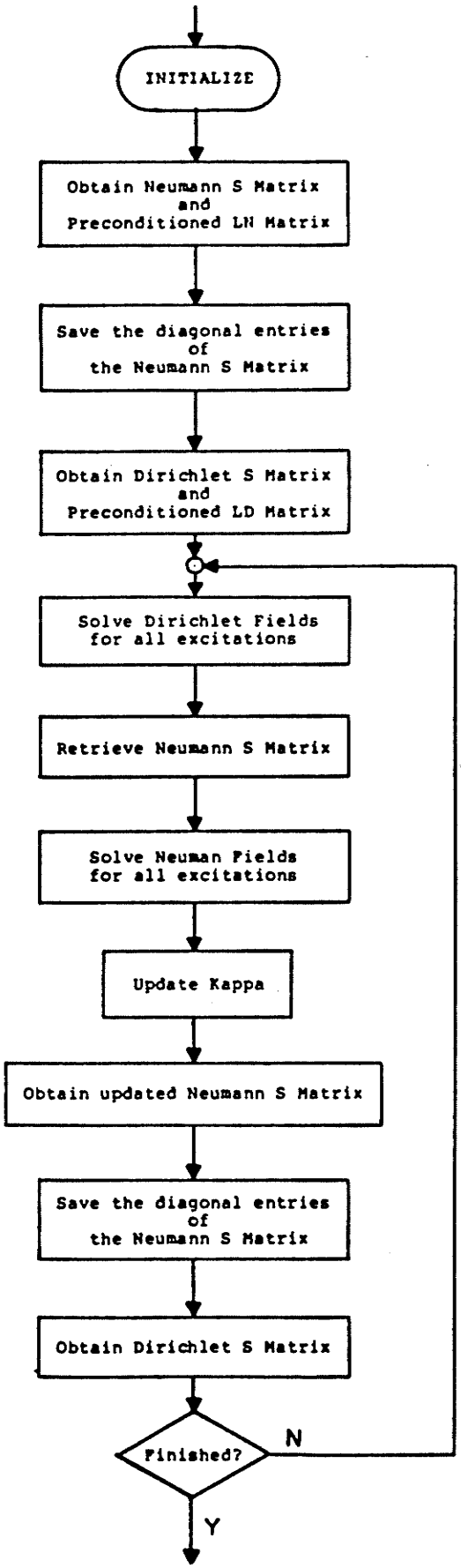

Figure 4.5: Imaging Algorithm Flowchart.

4.4 SIMULATION EXAMPLES

There are two methods of displaying recovered images; gray-level (density) shading and relief plots. In the figures that follow, density plots are presented for some of the two-dimensional images. In several diagrams corresponding relief diagrams are presented above the density plot for comparison. Based on experience, representing the conductivity value as the third dimension provides important information concerning recovered image edges and corners. In most figures the exact solution is displayed in the left-hand column and represents the ideal recovery.

In several two-dimensional cases, excitation patterns are below the recovered images. The lines superimposed on the grid structure indicate a particular input and output current site. In a general sense, they also relate to the current flow within the region, but by no means are they meant to indicate "beam-like" current path behaviour. Fig. 4.13 illustrates the effect of filtering a two-dimensional step function, a procedure which may be employed for edge discovery or enhancement purposes. Excitation patterns are similar in three-dimensional cases, except that some examples have excitations distributed over all sides, whereas other examples maintain top surface excitations and measurements only.

2-D Resistive Tomography Simulations

$$\kappa(x,y) = A \sin^2((x-2)/9*\pi)\sin^2((y-2)/7*\pi) + 1 \quad \left.\begin{array}{l} 2 \le x \le 11 \\ 2 \le y \le 9 \end{array}\right\}$$

$$\kappa(x,y) = 1 \quad \text{elsewhere}$$

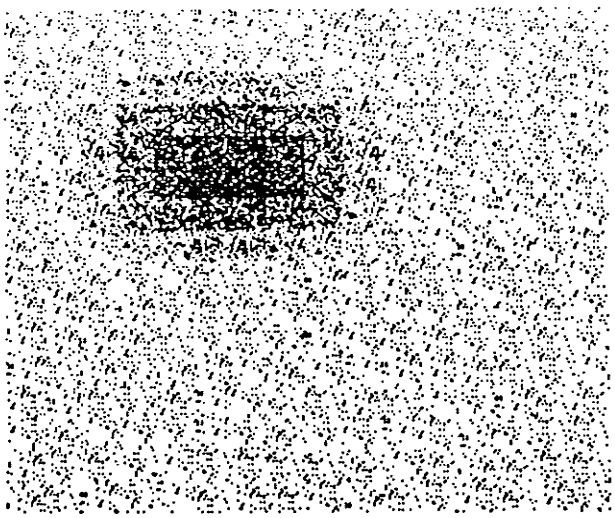

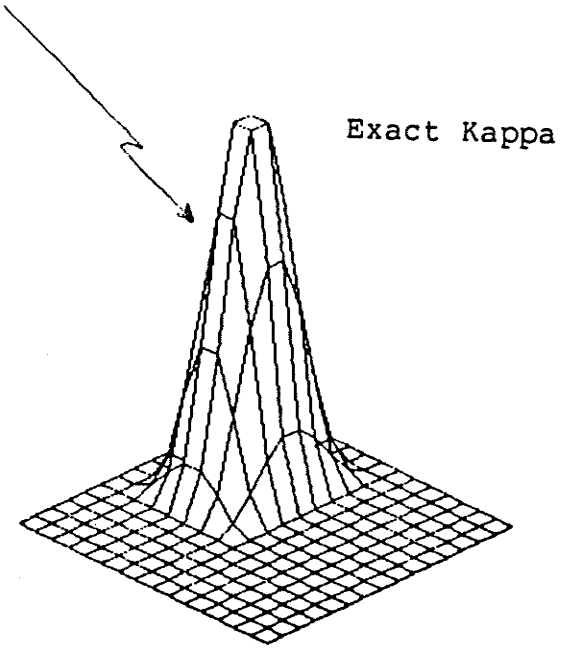

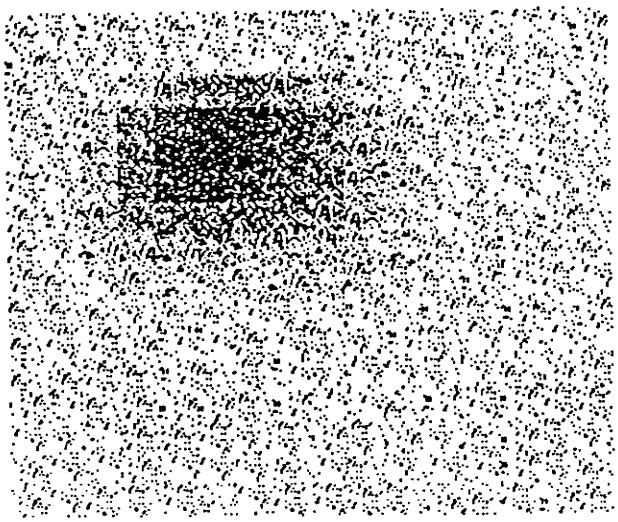

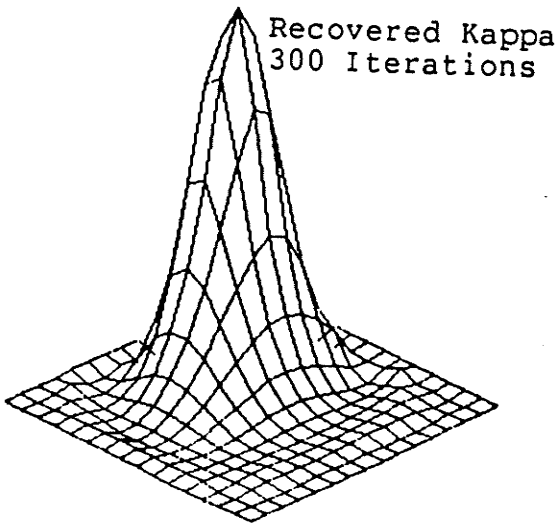

Figure 4.6: A Smoothly Varying Conductivity Distribution.

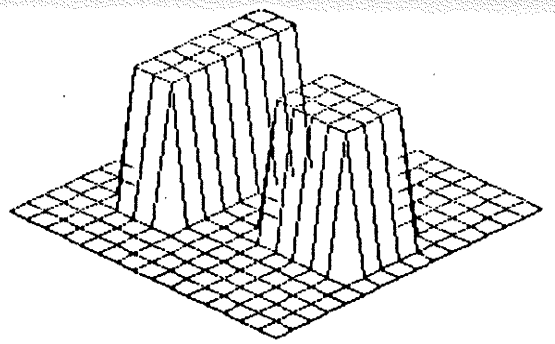

[A]

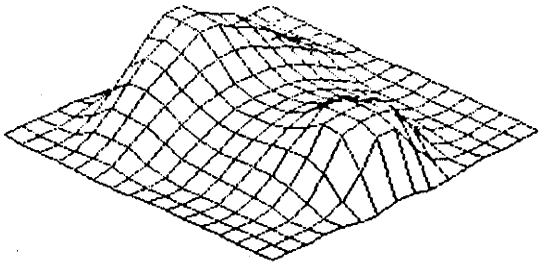

[C]

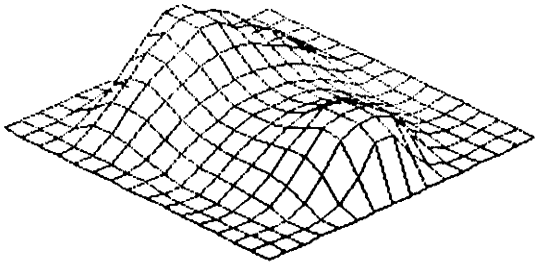

[E]

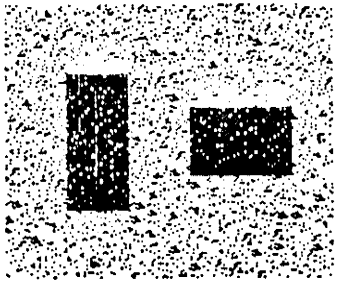

[B]

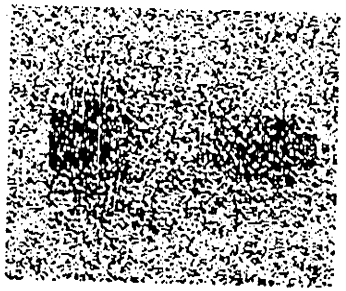

[D]

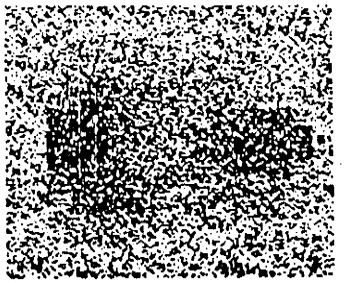

[F]

LEGEND

A. 3-D Representation - Exact Solution.
B. 2-D Density Plot - Exact Solution.
C. 3-D 10 Excitations & 50 Iterations.
D. 2-D 10 Excitations & 50 Iterations.
E. 3-D 20 Excitations & 50 Iterations.
F. 2-D 20 Excitations & 50 Iterations.
G. 10 Excitation Locations.
H. 20 Excitation Locations.

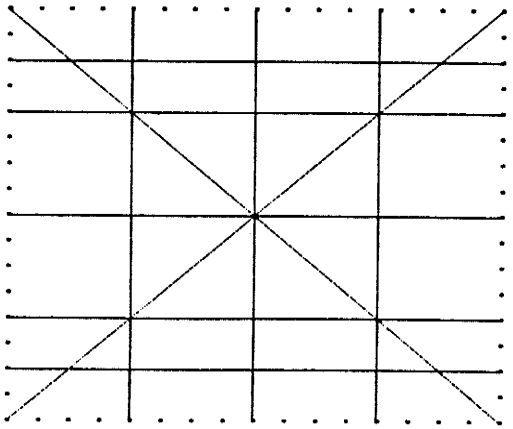

[G]

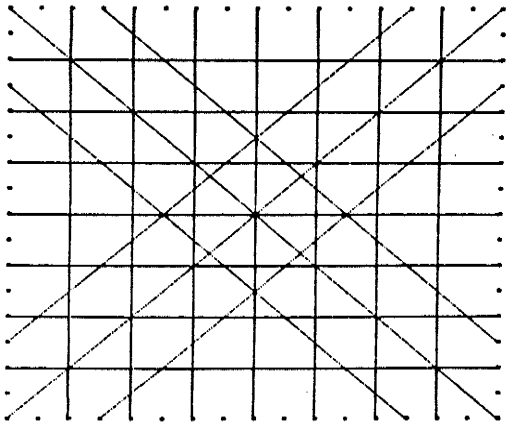

[H]

Figure 4.7: Two-Dimensional Split T after 50 Iterations.

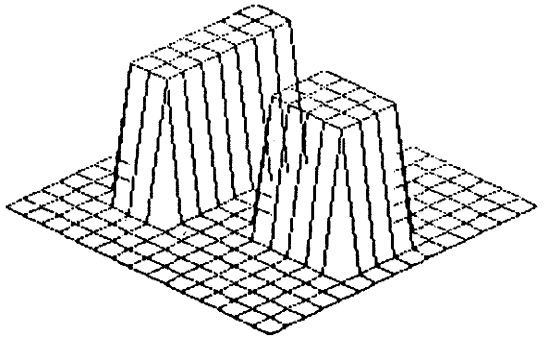

[A]

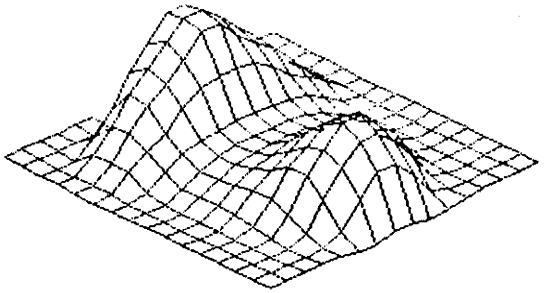

[C]

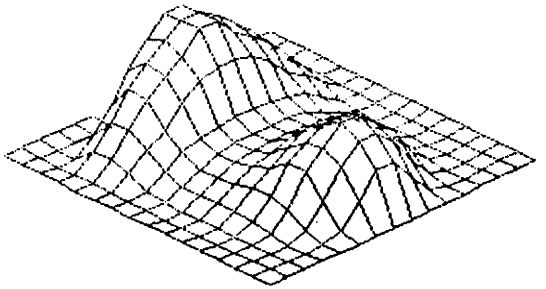

[E]

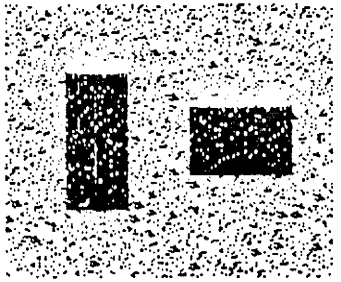

[B]

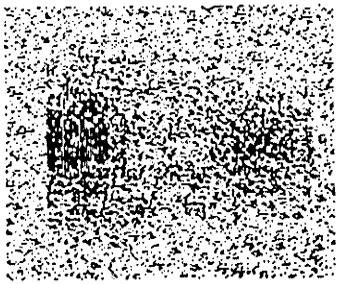

[D]

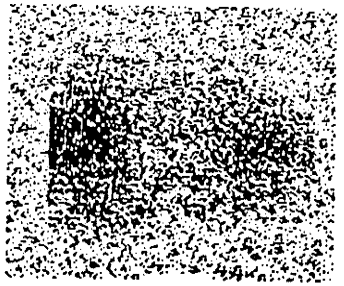

[F]

LEGEND

A. 3-D Representation - Exact Solution.
B. 2-D Density Plot - Exact Solution.
C. 3-D 10 Excitations & 100 Iterations.
D. 2-D 10 Excitations & 100 Iterations.
E. 3-D 20 Excitations & 100 Iterations.
F. 2-D 20 Excitations & 100 Iterations.
G. 10 Excitation Locations.
H. 20 Excitation Locations.

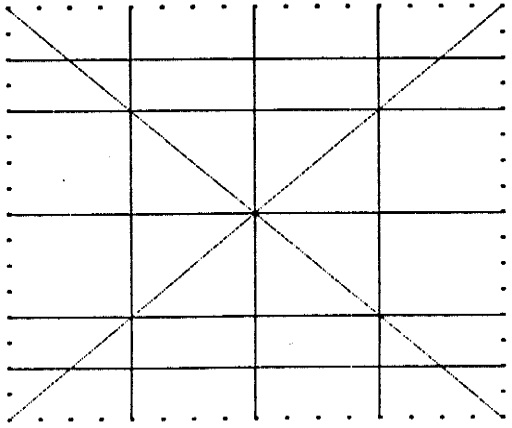

[G]

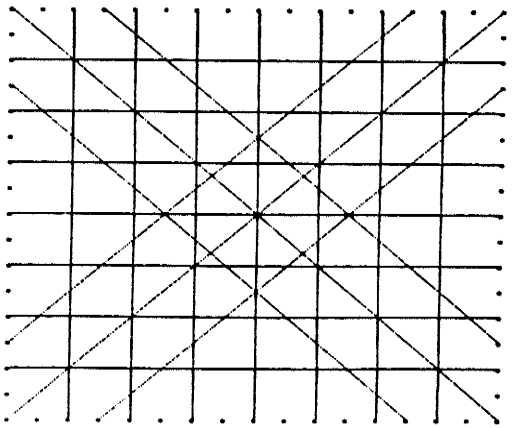

[H]

Figure 4.8: Two-Dimensional Split T after 100 Iterations.

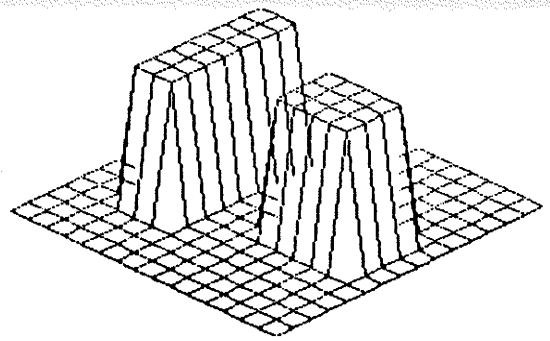

[A]

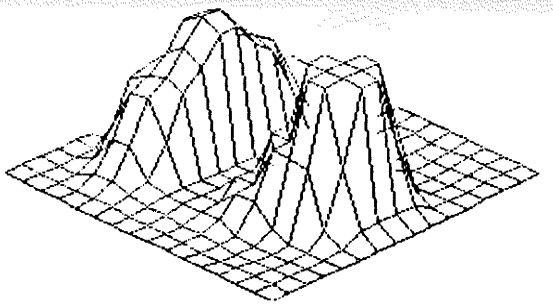

[C]

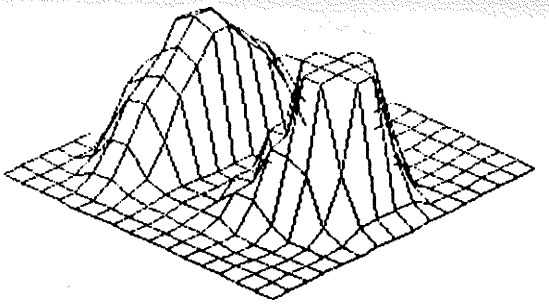

[E]

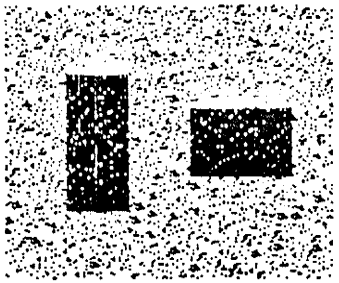

[B]

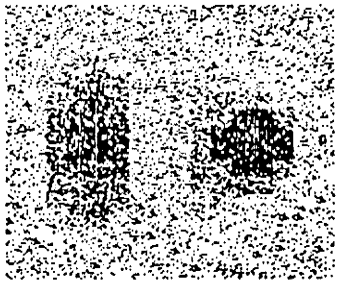

[D]

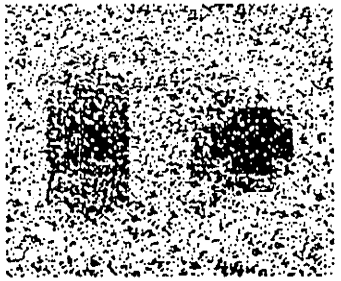

[F]

LEGEND

A. 3-D Representation - Exact Solution.
B. 2-D Density Plot - Exact Solution.
C. 3-D 10 Excitations & 500 Iterations.
D. 2-D 10 Excitations & 500 Iterations.
E. 3-D 20 Excitations & 500 Iterations.
F. 2-D 20 Excitations & 500 Iterations.
G. 10 Excitation Locations.
H. 20 Excitation Locations.

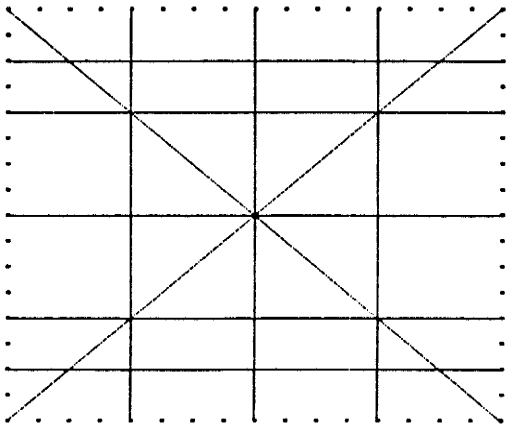

[G]

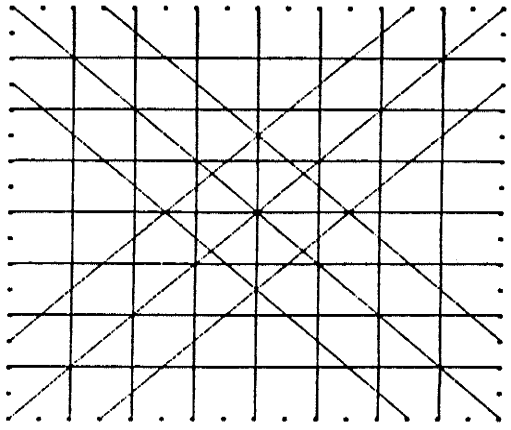

[H]

Figure 4.9: Two-Dimensional Split T after 500 Iterations.

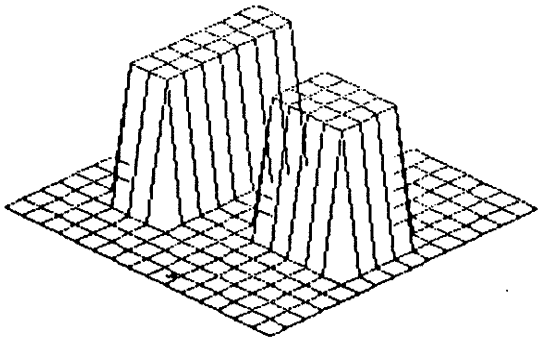

[A]

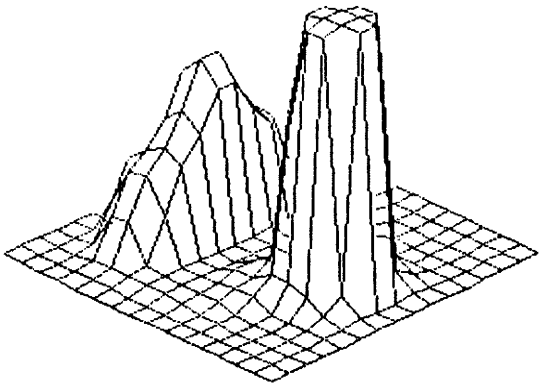

[C]

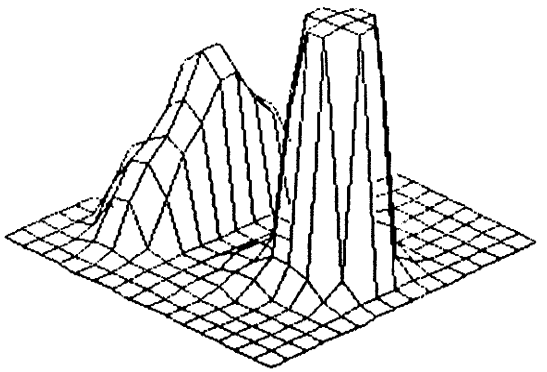

[E]

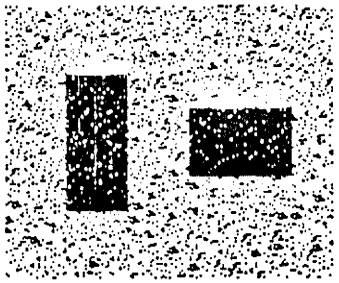

[B]

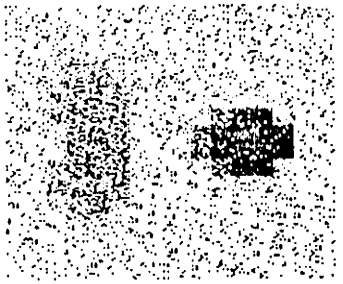

[D]

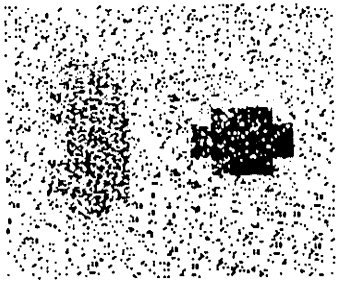

[F]

LEGEND

A. 3-D Representation - Exact Solution.
B. 2-D Density Plot - Exact Solution.
C. 3-D 10 Excitations & 1700 Iterations.
D. 2-D 10 Excitations & 1700 Iterations.
E. 3-D 20 Excitations & 1700 Iterations.
F. 2-D 20 Excitations & 1700 Iterations.
G. 10 Excitation Locations.
H. 20 Excitation Locations.

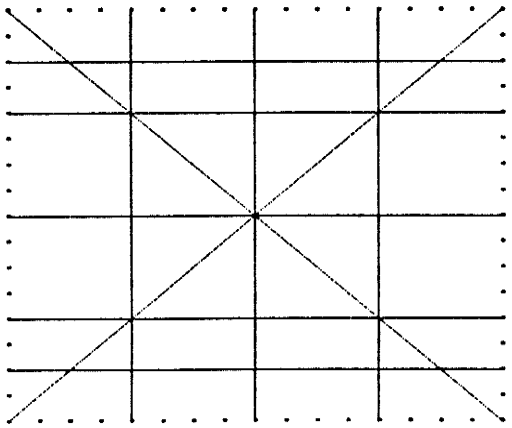

[G]

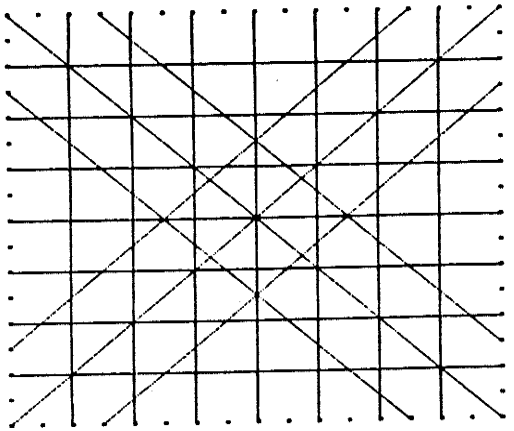

[H]

Figure 4.10: Two-Dimensional Split T after 1700 Iterations.

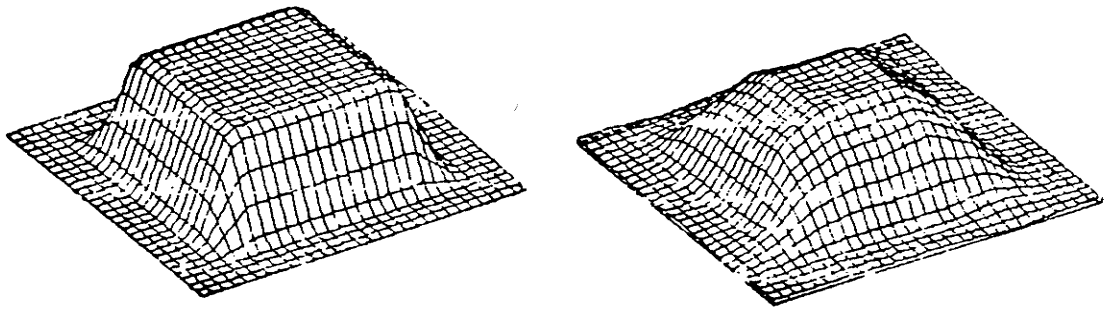

(a) Exact (b) Recovered

Figure 4.11: Recovery with Linear Conductance Elements.
6 Excitations 118 Iterations

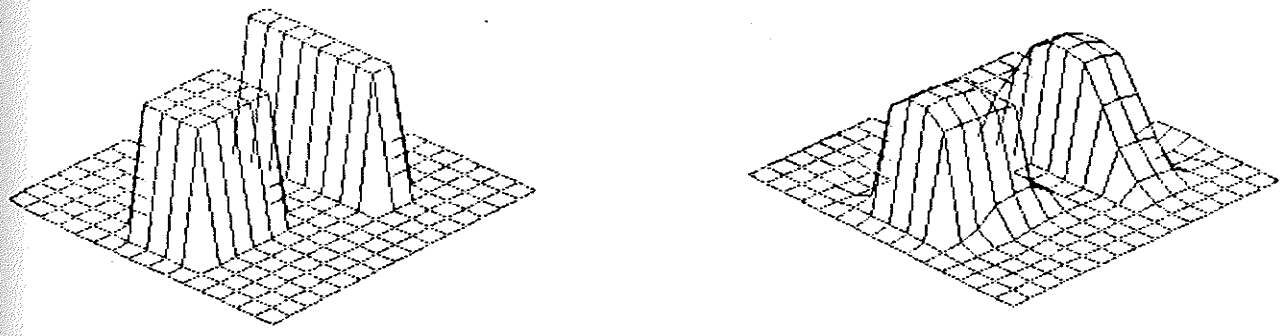

Figure 4.12: Recovery with Constant Conductance Elements.
10 Excitations 15,000 Iterations

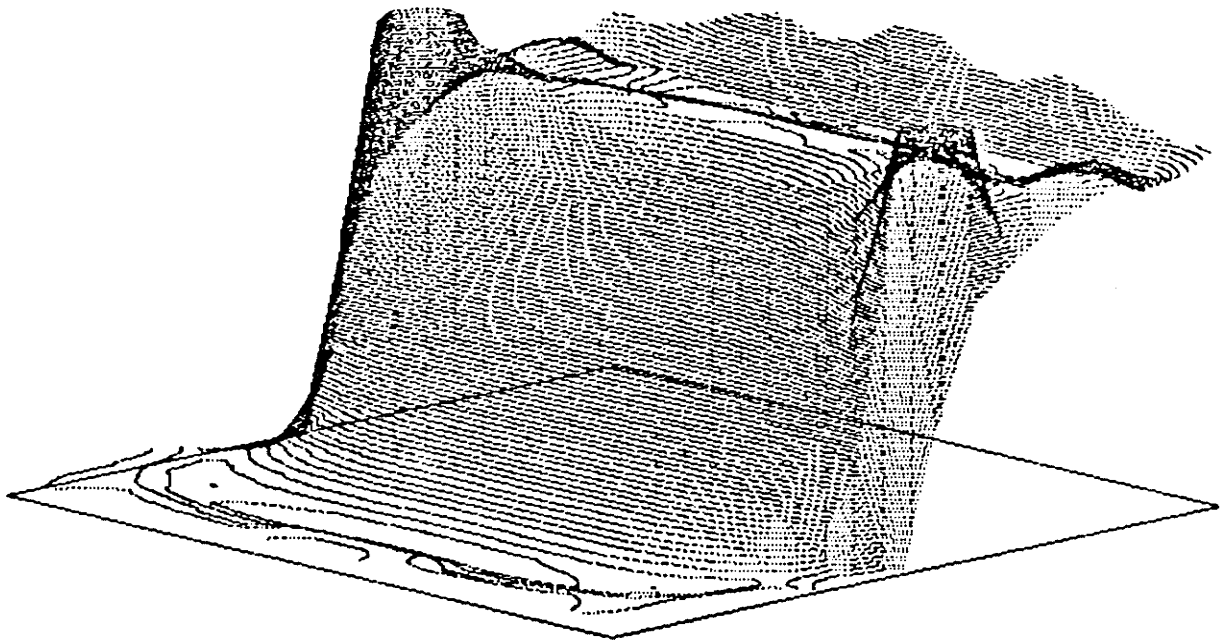

Figure 4.13: Hamming and Sobel Filtered Step Function.

Three-Dimensional Simulations

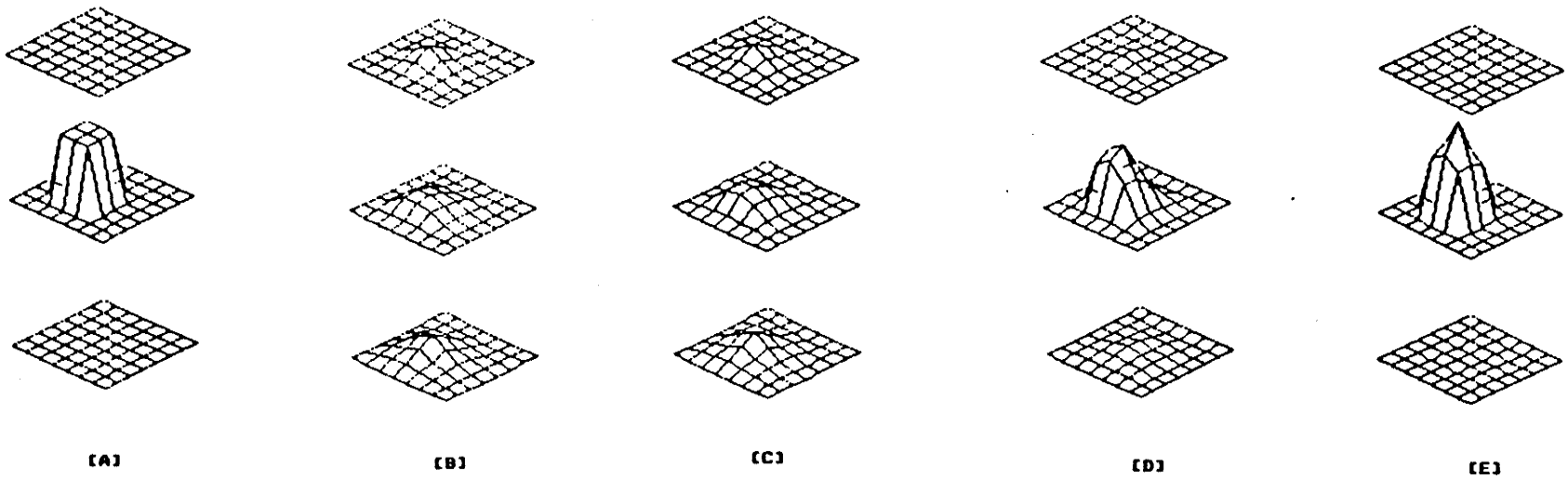

Figure 4.14: 3-D with Measurements Taken on All Sides.

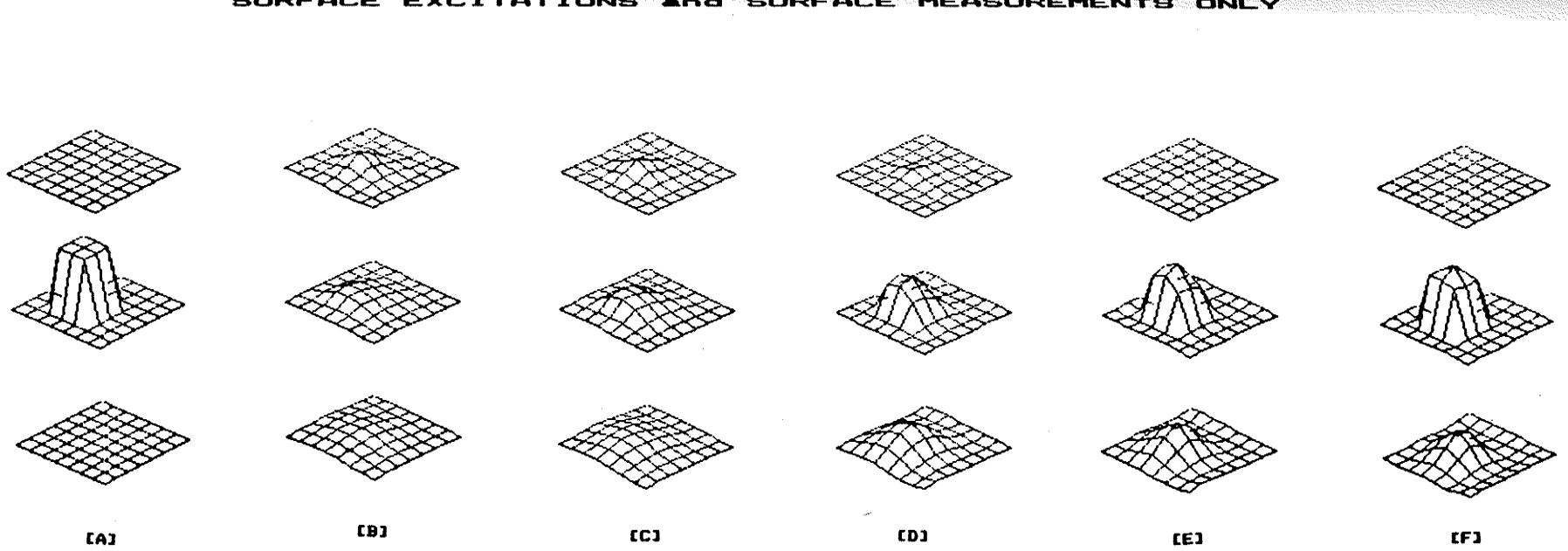

Figure 4.15: 3-D with Top Layer Measurements Only.

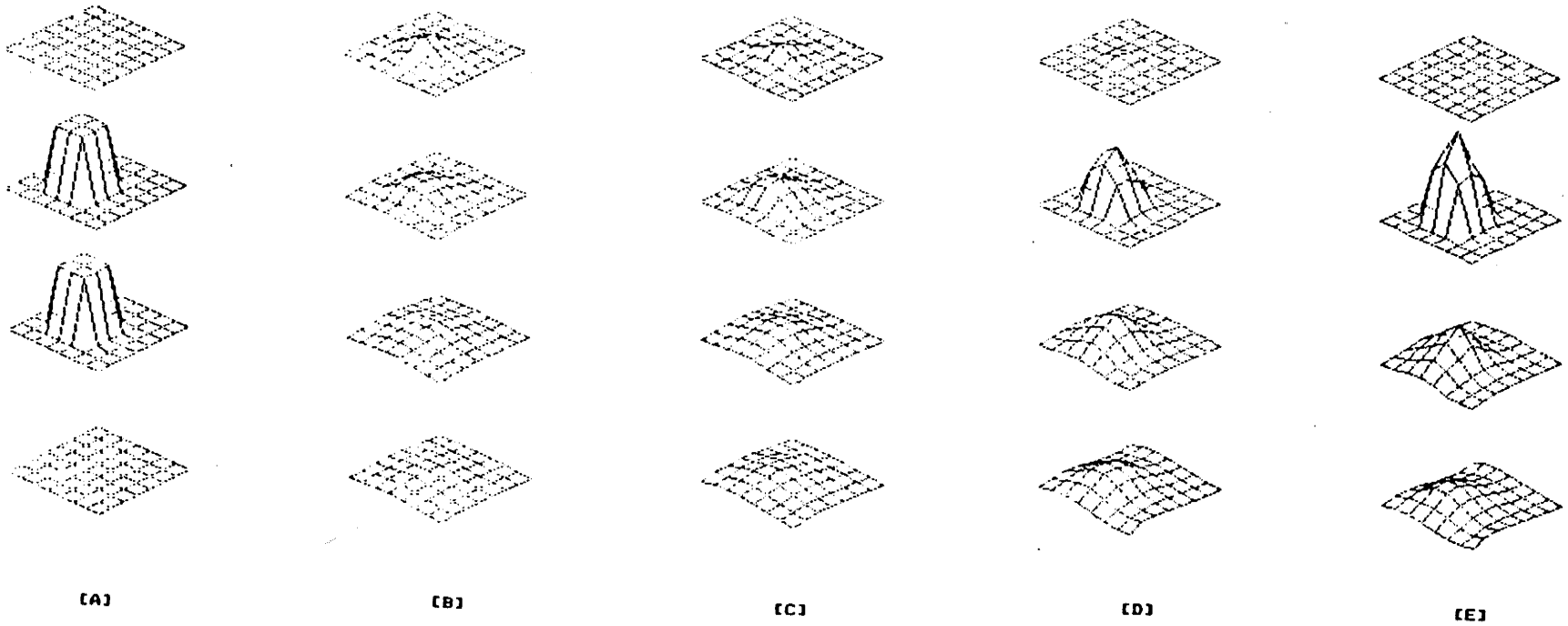

Figure 4.16: Four Layers with Surface Measurements.

Chapter V

DISCUSSION OF COMPUTER-SIMULATED IMAGING

A number of important questions are raised by the simulated imaging results of previous chapters. This chapter addresses some of these questions, including: quality of recovered solutions; number of measurements needed to obtain a solution; costs associated with imaging programs; and effects of modelling errors.

5.1 QUALITY OF RECOVERED SOLUTIONS

One important measure of success for any image reconstruction technique is the quality of the final solution. The density and height plots previously discussed clearly present differences between exact models and calculated solutions, and therefore represent a measure of quality. Another quality indicator is illustrated in Fig. 5.1(a), which displays a trace of the average difference per node between the calculated conductivity and the exact value at each iteration. If the iterative process is converging to the exact solution then this difference would be expected to approach zero. This was not the case however, as after only a few iterations the recovered conductivity settled to very slowly changing values (the drop at the tail end will be explained shortly).

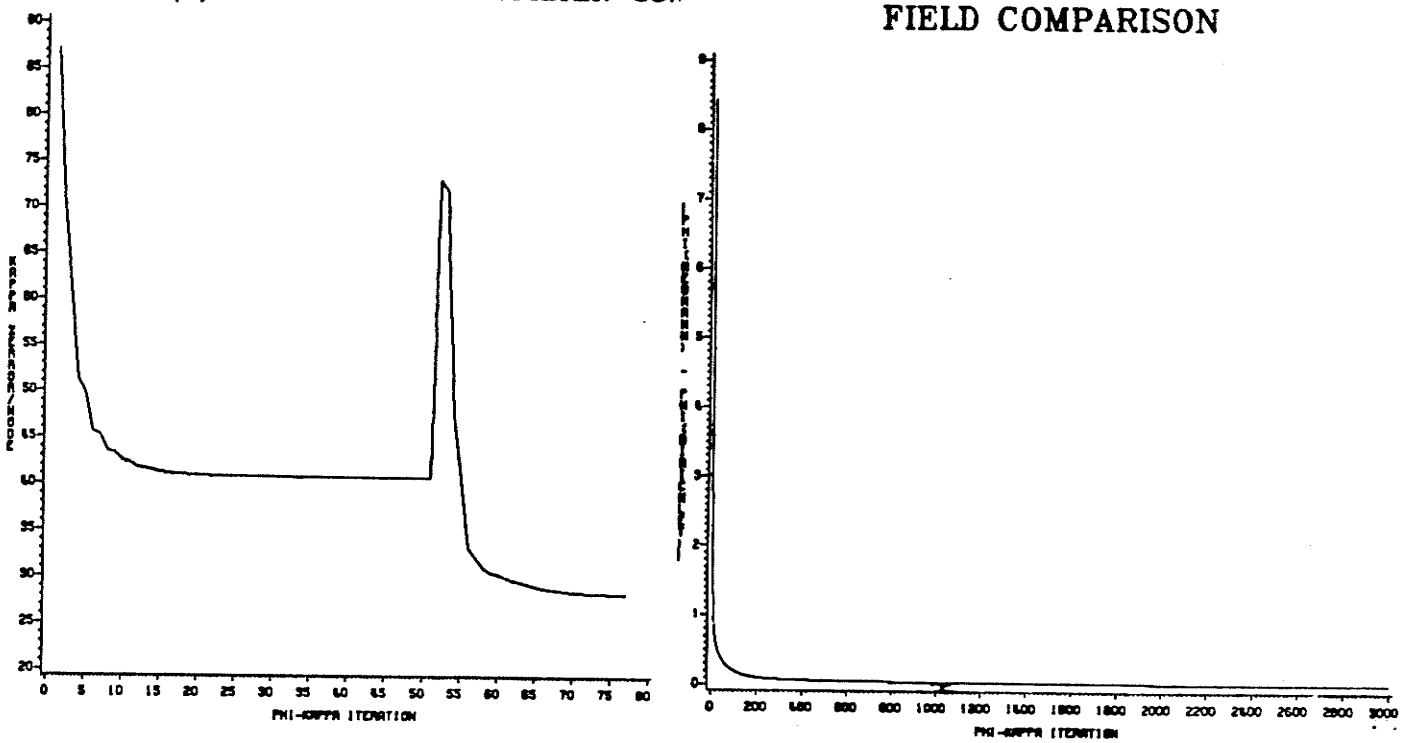

(a) (b)

Figure 5.1: Quality Indicators.

Once the conductivity has reached this "steady state" where only very small changes occur for each iteration, then an examination of the difference between Neumann and Dirichlet fields, Fig. 5.1(b), showed that both fields were almost identical. Furthermore, it turned out that although similar to each other, they were quite different from the exact field solution. Also, if the initial conductivity estimate happened to be identical to the exact solution then the iterative process was highly stable and exhibited only a small amount of drift.

The latter behaviour contradicts the former if the solution really is unique, and no proveable explanation has yet been found. Perhaps the method is stuck in an optimization-

like valley, or perhaps the gradient modelling is simply not of a high enough order. Another possibility is that at the low frequencies for which Laplace's equation is applicable, interior structures only influence the field within an extremely limited spatial extent. If this were true one possible solution would be to use higher excitation frequencies. At high frequencies the fields would be governed by Helmholtz's equation and the effects of small internal structures on the field would likely be noticeable even at large distances.

In any case, various filters were tried in order to eliminate high frequency oscillations. The tail end of Fig. 5.1(a) demonstrates that limited improvement is possible if the right filter is applied at the appropriate time.

The amount of current penetration in the region of interest also influences image quality. For instance, in Fig. (4.14) the bottom layer artifact eventually disappeared due to the inclusion of voltage measurements and current sites on that layer. Fig. 4.15 shows that without these lower layer measurements, the disappearance of the artifact requires more iterations. On the other hand, the second layer recovery is quite good. Because the measurements are only on the surface, those layers just below the surface tend to receive most of the current while the lower layers receive virtually no current. This would explain why the immediate sub-surface layers compare closely to those of the exact solution.

5.2 EXCITATION REQUIREMENTS

In order to clarify the relationship between the number of unknowns and the number of excitations, a particular finite element model must be examined (refer to Fig. 5.2). The example consists of an array of voxels (volume elements) measuring 3 by 3 by 3 and corresponding to a conductivity distribution. As well, a finite element node structure (4 by 4 by 4) is superimposed on the voxel array and is used in the electric field computation. It is from these nodes that all voltage measurements are taken or currents are injected.

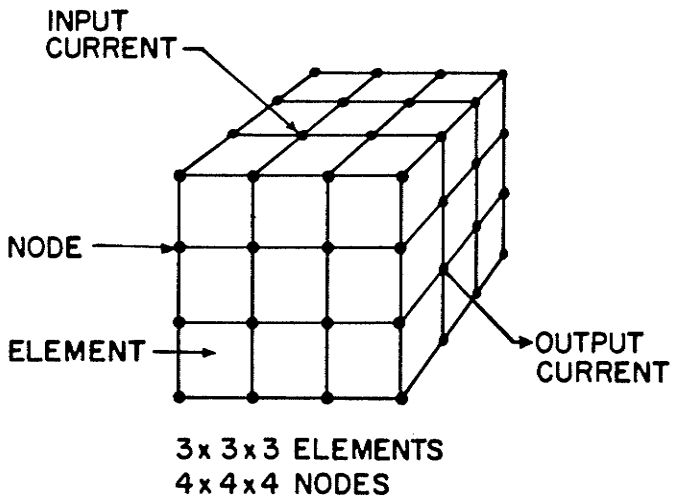

Figure 5.2: Typical Finite Element Structure.

Number of Voltage Measurements Required

From the above dimensions, the total number of nodes in the model is 64 while the total number of elements is 27. It should be noted that the total number of unknowns is equal to the number of conductivity elements (voxels). If medical applications are considered, then due to physical limitations the only accessible nodes -- for measurement or injection purposes -- are those on the front, back and side surfaces. Thus, the maximum number of accessible nodes is 48.

Based on the assumption that a reasonable solution requires twice as many voltage measurements as there are unknowns, the number of voltage measurements needed are 54.

Satisfying the Measurement Criterion

If there are N accessible electrodes and N1 current sites, then there are (N1-1) unique excitations and N electrodes at which voltage measurements can be taken. The total number of measurements is found by multiplying the number of available electrodes by the number of unique excitations, N*(N1-1). For example, consider the following excitation alternatives:

i) Let N=48 (number of accessible electrodes) and choose N1=3 (number of current sites). Thus, there are N1-1=2 unique excitations and N=48 valid voltage measurement locations per excitation, and therefore 48*2=96 measurements in total.

ii) Let N=12 (number of accessible electrodes) and choose N1=6 (number of current sites). Thus, there are N1-1=5 unique excitations and N=12 valid voltage measurement locations per excitation, and therefore 12*5=60 measurements in total.

The second choice may arise due to physical constraints on electrode spacing, or economic constraints on the cost of measurement apparatus. If the allowable number of voltage measurement probes decreases, a suitable increase in the number of excitations will compensate. Note: although both schemes yield approximately the necessary number of measurements, there is a significant difference in the number of unique excitations between the two alternatives. This is a very important point to consider as the number of excitations to be solved will ultimately determine the nature of the imaging hardware.

5.3 PROGRAM REQUIREMENTS

Storage Needs

Listed below are the computer memory allocations needed to perform imaging on a machine with either single or multi-processing capabilities. Multi-processing is important because the imaging process is highly parallel, and is therefore well suited to concurrent processing of the computations required for each excitation. Although multi-processing was not used in these tests, all programs were organized and structured for this eventuality.

The storage allocations may be partitioned into three areas:

i) Common Store - This consists of data that is stored in the main system memory and freely accessed by any other program or processor on the system. The 3-D problem previously discussed requires about 186,000 bytes of common store.

ii) Dirichlet Store - A multi-processing machine could perform this calculation simultaneously for all excitations, thus enhancing throughput. Such a system would perform the calculation on local processors dedicated to each excitation. Approximately 131,040 bytes are needed to accomodate each excitation. A single processor machine -- similar to that used for the tests in this thesis -- still needs the same amount of store, but utilizes the excitations one at a time.

iii) Neumann Store - This calculation could also be performed simultaneously for all excitations. The calculation may be carried out by a local processor using local storage only, or by a single processor operating on each excitation one at a time. Approximately 124,488 bytes will be needed.

Estimate of Imaging Program CPU Time

The most time-consuming section of code in the imaging algorithm occurs within the electric field computations. In particular, a multiplication is significantly more time-consuming than any other simple arithmetic operation, and since multiplications dominate the field computations, the following timing estimates are based on the number of multiplications executed. Comparisons are included which demonstrate the difference between a high-performance mainframe (AMDAHL V7) and a high-performance microcomputer (8086/8087). The mainframe computer is only capable of performing sequential operations. The microcomputer is treated as both a sequential and a parallel machine. Note: all timings are based on the CPU cycle time for a single multiplication and do not take into account various system overhead costs. It is expected that the actual timings would be greater than those listed by a factor between 1 and 2.

The number of multiplications for one iteration of the imaging algorithm can be expressed as follows:

$$M=(2K-3)U+(1-K)+C[4U(K+1)+(1-K)]$$

where M is the number of multiplications; K is the matrix bandwidth; U is the number of unknowns; and C is the number of field solution iterations.

The following timings assume:

C=10 K=14 U=1683 I=Number of Imaging Iterations

	AMDAHL	8086/8087	
1 multiply	250ns.	19us.	
I=1	2.8s.	3.5m.	(Sequential)
		6.5s.	(Parallel)
I=3	8.3s.	10.5m.	(Sequential)
		19.7s.	(Parallel)
I=10	27.6s.	35.0m.	(Sequential)
		65.0s.	(Parallel)
I=50	138.0s.	174.8m.	(Sequential)
		5.5m.	(Parallel)

5.4 EFFECTS OF MODELLING ERRORS

Problem Geometry

Consider a small "tube" of distributed conductivity as in Fig. 5.3

where

$$I(x,y,z) = J(x,y,z) \times S \ . \qquad (5.1)$$

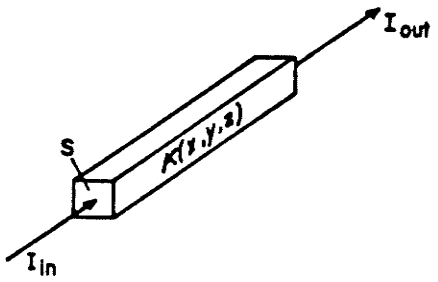

Figure 5.3: Distributed Conductivity.

Now imagine the surface area S gradually reducing so that the problem virtually becomes unidimensional (Fig. 5.4)

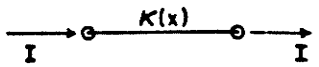

Figure 5.4: One-Dimensional Model.

where

$$I(x) = J(x) \times S \ . \qquad (5.2)$$

For example, if we take

$$S = \frac{1}{100} \times \frac{1}{100} = 10^{-4} m^2 = 1 \text{ cm}^2$$

$$I(x) = .1 \text{ ma} \tag{5.3}$$

then

$$J(x) = \frac{I(x)}{S} = \frac{.1 \text{ ma}}{1 \text{ cm}^2} = 1.0[A/m^2] \; . \tag{5.4}$$

Now consider such a quasi-one-dimensional region defined from x=0.0 to x=2.0, and choose

$$\kappa(x) = \frac{x+2}{2} \tag{5.5}$$

and

$$f(x) = 0.0 \tag{5.6}$$

throughout the region. Next, since

$$\bar{J} = \kappa \bar{E} = -\kappa \nabla \phi \tag{5.7}$$

becomes

$$\bar{J} = -\kappa \frac{d\phi}{dx} \tag{5.8}$$

we have

$$\frac{d\phi}{dx} = \frac{-J(x)}{\kappa(x)} = \frac{-1.0}{\frac{x+2}{2}} = \frac{-2.0}{x+2} \quad . \tag{5.9}$$

Thus the problem is simplified to that illustrated in Fig. 5.5.

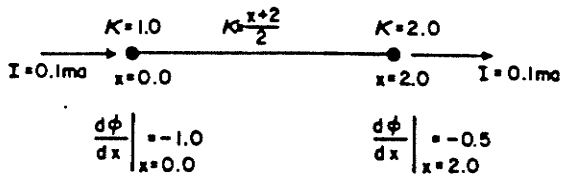

Figure 5.5: Simplified Problem Description.

Integrating (5.9)

$$\phi(x) = -2\ell n(x+2) + c_1 \tag{5.10}$$

and for convenience, taking the zero reference at x= -1.0 and applying this as a boundary condition, yields

$$\phi(x)\Big|_{x=-1} = 0 = -2\ell n(-1+2) + c_1 \rightarrow c_1 = 0 \ . \tag{5.11}$$

Therefore

$$\phi(x) = -2\ell n(x+2) \ . \tag{5.12}$$

Recovering the Conductivity

The point-iterative algorithm used to recover the conductivity -- given the field gradient distribution -- in one dimension is

$$\kappa_i = \frac{-\int \alpha_i J_x \frac{d\phi}{dx}\, dx - \sum_{j,j\neq i} \int \alpha_i \alpha_j \left(\frac{d\phi}{dx}\right)^2 dx\, \kappa_j}{\int \left(\alpha_i \frac{d\phi}{dx}\right)^2 dx} \ . \tag{5.13}$$

To evaluate (5.13) we must solve several integrals. These are found through application of Gaussian quadrature. Since this requires the integrands to be evaluated only at Gauss points, we may discretize the problem as in Fig. 5.6.

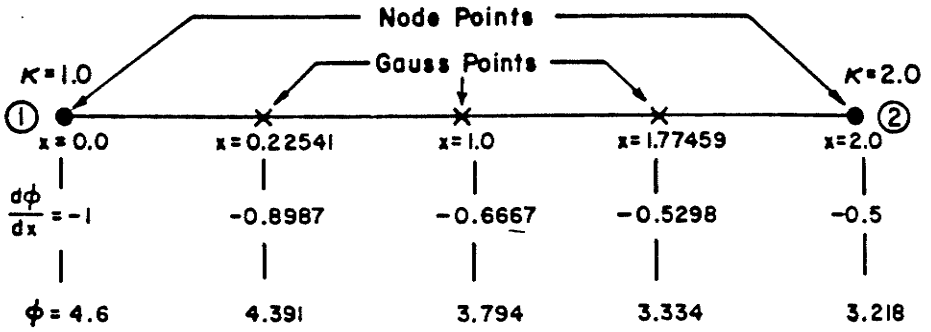

Figure 5.6: Discretized Problem.

Linear Lagrangian Shape Functions

The simplest interpolation functions are linear, and are usually defined over the standard region from x= -1.0 to x=1.0. In a straightforward manner these shape functions are transformed from standard to arbitrary regions. The appropriate definitions pertinent to Fig. 5.6 are

$$\alpha_1 = \frac{2-x}{2} \qquad (5.14)$$

$$\alpha_2 = \frac{x}{2} \quad .$$

Analytic Lagrangian Recovery for Node 1

Assuming that the values of all field gradients -- evaluated at the Gauss points -- are available, and using the analytic expression for the field gradient (5.9) and the current density (5.4), the recovered conductivity at node 1 may be found from (5.13)

$$\kappa_1 = \frac{-\int \alpha_1 J_x \frac{d\phi}{dx}\, dx - \int \alpha_1 \alpha_2 (\frac{d\phi}{dx})^2 dx\, \kappa_2}{\int (\alpha_1 \frac{d\phi}{dx})^2 dx} \quad . \tag{5.15}$$

Substituting where appropriate, (5.15) becomes

$$\kappa_1 = \frac{-\int_0^2 (\frac{2-x}{2})(1.0)(\frac{-2}{2+x})dx - \int_0^2 (\frac{2-x}{2})(\frac{x}{2})(\frac{-2}{2+x})^2 dx(2)}{\int_0^2 (\frac{2-x}{2})^2 (\frac{-2}{2+x})^2 dx} \tag{5.16}$$

$$= \frac{(4\ell n2-2) + (8-12\ell n2)}{6-9\ell n2} = \frac{.772589 - .317766}{.454823} = 1.0$$

as expected when the exact field gradients are used.

Numerical Lagrangian Recovery

To evaluate (5.15) numerically, it must be observed that since we are using a linear interpolation scheme, the field gradient is now approximated throughout the element by the value of the middle Gauss point (refer to Fig. 5.6)

$$\frac{d\phi}{dx} = - .6667 \ . \tag{5.17}$$

Using this value in (5.15) rather than the analytically derived value yields

$$\kappa_1 = \frac{-\int_0^2 (\frac{2-x}{2})(-.6667)dx - \int_0^2 (\frac{2-x}{2})(\frac{x}{2})(.6667)^2 dx(2)}{\int_0^2 [(\frac{2-x}{2})(-.6667)]^2 dx} \tag{5.18}$$

$$= \frac{.66667 - .2963}{.2697} = 1.37$$

which ought to be compared against (5.16). The error arises due to the attempt to approximate a complicated gradient curve with a linear function. This demonstrates the necessity for either a higher-order approximation or more linear elements within the same region.

Chapter VI

CONCLUSIONS

This thesis has presented a new method for reconstructing distributions of electrical conductivity from sets of potential measurements taken over the boundaries. An iterative least-squares technique -- which employed a combination of point-iterative and pre-conditioned conjugate gradient methods -- was applied to both two and three-dimensional field problems as well as to resistance networks. Several test programs were run and example solutions were presented for both field and network problems.

The proposed conductivity recovery procedure is shown to be fundamentally different from the usual impedance computed tomography (ICT) approach. Impedance imaging has, until now, been no more than an extension of normal X-ray projection methods. Indeed, several key ICT researchers [Lytle, Price, Schomberg] attempted to force beam-like current flow so that projection techniques could be accomodated in their impedance imaging tests. Their lack of significant progress is likely due to limitations inherent in the projection process.

As discussed earlier, arguments have been put forward [Bates et al] which proved that conductivity distributions

could not be successfully recovered using the projection approach common to X-ray tomography. The algorithm suggested here avoids such difficulties by allowing current to follow a natural path rather than forcing beam-like behaviour. As a consequence boundary measurement values are shown to be influenced by the conductivity of the entire region. It is further demonstrated how to employ these boundary measurements, which are not projections, in such a way as to move each iterative step in the direction of the proper solution.

The inversion scheme is shown to involve a decoupling of the basic nonlinear system into three linear subsystems which are then solved simultaneously. For inhomogeneous media problems each successive conductivity estimate involves a least-squares conductivity calculation based on a residual acquired from the point form of Ohm's law; a current density approximation obtained by first solving Laplace's equation under Neumann boundary conditions and then multiplying the gradient of this field by the previous conductivity estimate; and an electrostatic potential gradient approximation obtained from a field which satisfies Laplace's equation under Dirichlet boundary conditions.

For potential field calculations the Rayleigh-Ritz discretization procedure is applied to the energy functional. If computer memory storage is at a premium system matrix entries are generated node by node and immediately applied, thus implementing a point-iterative technique. However,

since the potential field calculation is itself iterative, the cost associated with generating system matrix entries during each iteration may be prohibitive. If so, then the entire system matrix is accumulated prior to finding the field solution, and a pre-conditioned conjugate gradient method is used instead.

Appendix A

THE POINT-ACCUMULATIVE, POINT-ITERATIVE METHOD

A.1 INTRODUCTION

A linear system of equations -- as derived from finite element discretization techniques -- can be solved by a point-iterative process. Until recently, the practice has been to solve these systems using direct sparsity methods such as Zollenkopf bifactorization [37,38]. Most often, direct techniques are cumbersome to implement and usually they impose serious restrictions on execution time and main storage requirements. Large problems, such as those involving three-dimensional fields, can only be solved directly by resorting to intricate programming strategies [39]. The algorithm presented in this Appendix however, requires minimal programming effort and maintains all advantages (i.e. rapid execution and reduced memory requirements) inherent in relaxation based methods [40].

Consider the generalized differential operator equation

$$L\psi = f \tag{A.1}$$

where L is self-adjoint and positive definite. The source distribution for the field ψ is defined by f. Applying standard discretization techniques, the linear system

$$S\underline{\psi} = \underline{b} \tag{A.2}$$

is generated. In particular, application of the point-iterative scheme to the steady state Laplacian equation

$$-\nabla \cdot (\overline{\overline{p}} \cdot \nabla\psi) = f \qquad \text{(A.3)}$$

is discussed in detail.

Square-shaped two-dimensional elements and cube-shaped three-dimensional elements have been implemented over a regular grid, and theoretical considerations for both types are discussed.

A.2 VARIATIONAL FORMULATION

The variational principle [41,42] states that the solution of equation (A.1) can be obtained by minimizing the functional

$$F = < L\psi , \psi > - 2 < f , \psi > \qquad \text{(A.4)}$$

where the bracketed terms denote appropriately defined inner products.

Through the use of Green's theorem equation (A.4) becomes

$$F = \int_{\Omega} (\nabla\psi) \cdot \overline{\overline{p}} \cdot (\nabla\psi) dv - 2 \int_{\Omega} f\psi \, dv \qquad \text{(A.5)}$$

and, as stated, is only valid for the Dirichlet

$$\psi\Big|_s = g(s) \tag{A.6}$$

and homogeneous Neumann

$$\hat{n} \cdot \nabla\psi = 0 \tag{A.7}$$

boundary conditions. More general functionals are available [43] for more complicated boundary conditions.

Discretizing ψ by the Rayleigh-Ritz procedure

$$\psi = \underline{\alpha}^T \underline{\psi} = \underline{\psi}^T \underline{\alpha} \tag{A.8}$$

and substituting (A.8) into (A.5) while enforcing

$$\frac{\partial F}{\partial \underline{\psi}} = \underline{0} \tag{A.9}$$

results in the linear system of (A.2) where

$$S = \int_\Omega (\nabla\underline{\alpha}) \cdot \overline{\overline{p}} \cdot (\nabla\underline{\alpha}^T) dv \tag{A.10}$$

and

$$b = \int_{\Omega} f\underline{\alpha}\, dv \quad . \tag{A.11}$$

The integrals specified by S and $\underline{b}$ are first evaluated numerically for a single finite element, and subsequently accumulated on an element by element basis -- in a fashion parallel to the finite difference SOR technique -- to form a "virtual" global system matrix. In practice, the entire global matrix is not stored as all accumulations are performed only when required by the iteration algorithm.

A.3 MATRIX GENERATION

Using a double subscript convention, equation (A.2) may be rewritten as

$$\sum_j S_{ij}\, \psi_j = S_{ij}\, \psi_j = b_i \tag{A.12}$$

where

$$S_{ij} = \int_{\Omega} (\nabla\alpha_i) \cdot \overline{\overline{p}} \cdot (\nabla\alpha_j) dv \tag{A.13}$$

and

$$b_i = \int_\Omega f\alpha_i \, dv \, . \tag{A.14}$$

Modelling the media by the same finite element structure used for the field allows $\bar{\bar{p}}$ to be expressed as

$$\bar{\bar{p}} = \bar{\bar{\alpha}} \cdot \underline{p} = \bar{\bar{\alpha}}^T \cdot \underline{p} = \bar{\bar{\alpha}}_k \, p_k \quad . \tag{A.15}$$

Substituting (A.15) into (A.13), and factoring out $\underline{p}$ yields

$$S_{ij} = \int_\Omega \vec{\beta}_i \cdot \bar{\bar{\alpha}}^T \cdot \vec{\beta}_j \, dv \, \underline{p} \tag{A.16}$$

with the spatial vector $\vec{\beta}$ representing the gradient of the scalar shape functions. An equivalent expression is

$$S_{ij} = \int_\Omega \vec{\beta}_i^T (\bar{\bar{\alpha}}^T)^T \vec{\beta}_j \, dv \, \underline{p} \tag{A.17}$$

which may also be written as

$$S_{ij} = \int_\Omega \beta_{i\ell} (\alpha_{k\ell m} \beta_{mj}) dv \, p_k \tag{A.18}$$

or

$$S_{ij} = S^*_{ijk}\, p_k \quad . \tag{A.19}$$

The source terms (A.14) may be factored as

$$b_i = B^*_{ij}\, f_j \tag{A.20}$$

where

$$B^*_{ij} = \int_{\Omega} \alpha_i \alpha_j \, dv \, . \tag{A.21}$$

It is important to observe that S* and B* are dependent only on the choice of α and not on the media or source characteristics.

With the finite element method, the interpolation functions used in (A.18) and (A.21) need only be defined over localized domains [44]. These functions are constructed from an elementary basis which is defined in two parts: for linear elements

$$\{L^1_1(x) \, , \, L^1_2(x) \,|\, L^1_1 \equiv \frac{1-x}{2} \, ; \, L^1_2 \equiv \frac{1+x}{2} \, ; \, -1 \leq x \leq 1\} \tag{A.22}$$

and for quadratic elements

$$\{L_1^2(x),\ L_2^2(x),\ L_3^2(x) \mid L_1^2 \equiv \frac{x(x-1)}{2};\ L_2^2 \equiv 1-x^2;\ L_3^2 \equiv \frac{x(x+1)}{2};\ -1 \leq x \leq 1\}\ . \quad (A.23)$$

The node numbering scheme displayed in Fig. A.1 leads to the scalar shape functions listed in Table A.1.

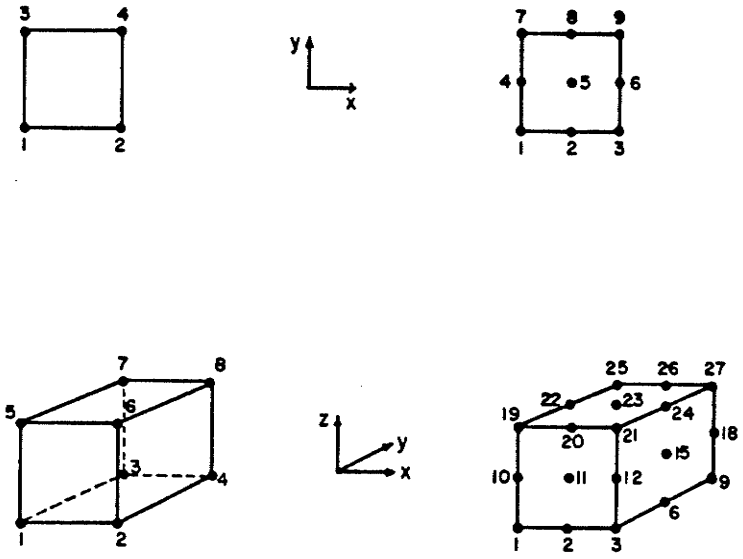

a) Linear

b) Quadratic

Figure A.1: Node Numbering

TABLE A.1

Scalar Shape Functions

SET	COORDINATE RANGE	n	$\alpha_n(\vec{r})$
2D LINEAR	i,j=1,2	2(j-1) + i	$L_i^1(x)\,L_j^1(y)$
3D LINEAR	i,j,k=1,2	4(k-1)+2(j-1)+i	$L_i^1(x)L_j^1(y)L_k^1(z)$
2D QUADRATIC	i,j=1,3	3(j-1)+ i	$L_i^2(x)L_j^2(y)$
3D QUADRATIC	i,j,k=1,3	9(k-1)+3(j-1)+i	$L_i^2(x)L_j^2(y)L_k^2(z)$

Any scalar set may be represented as

$$\underline{\alpha} = \begin{bmatrix} \alpha_1 \\ \alpha_2 \\ \cdot \\ \cdot \\ \cdot \\ \alpha_n \end{bmatrix} \tag{A.24}$$

and the tensor as

$$\underline{\underline{\alpha}} = \begin{bmatrix} \underline{\alpha} & \underline{\alpha} & \underline{\alpha} \\ \underline{\alpha} & \underline{\alpha} & \underline{\alpha} \\ \underline{\alpha} & \underline{\alpha} & \underline{\alpha} \end{bmatrix} = \begin{bmatrix} \vec{\alpha}_1 & \vec{\alpha}_{28} & \vec{\alpha}_{55} \\ \vdots & \vdots & \vdots \\ \vec{\alpha}_{27} & \vec{\alpha}_{54} & \vec{\alpha}_{81} \\ \vec{\alpha}_{28} & \vec{\alpha}_{82} & \vec{\alpha}_{109} \\ \vdots & \vdots & \vdots \\ \vec{\alpha}_{54} & \vec{\alpha}_{108} & \vec{\alpha}_{135} \\ \vec{\alpha}_{55} & \vec{\alpha}_{109} & \vec{\alpha}_{136} \\ \vdots & \vdots & \vdots \\ \vec{\alpha}_{81} & \vec{\alpha}_{135} & \vec{\alpha}_{162} \end{bmatrix}$$

$$= \underline{\alpha}\,\hat{u}_x\hat{u}_x + \underline{\alpha}\,\hat{u}_x\hat{u}_y + \underline{\alpha}\,\hat{u}_x\hat{u}_z + \underline{\alpha}\,\hat{u}_y\hat{u}_x + \underline{\alpha}\,\hat{u}_y\hat{u}_y + \underline{\alpha}\,\hat{u}_y\hat{u}_z + \underline{\alpha}\,\hat{u}_z\hat{u}_x + \underline{\alpha}\,\hat{u}_z\hat{u}_y + \underline{\alpha}\,\hat{u}_z\hat{u}_z \tag{A.25}$$

where for orthotropic media there are at most six independent tensor components.

Once a set from Table A.1 has been specified, the local finite element matrices, S* and B*, are calculated using numerical integration. As an example, consider a particular integral from S* for an inhomogeneous orthotropic media modelled by quadratic elements

$$S^*_{ijk} = S^*_{26,16,101} \cdot \tag{A.26}$$

From (A.24) and (A.25)

$$\begin{aligned} \alpha_i &= \alpha_{26} \\ \alpha_j &= \alpha_{16} \\ \overline{\overline{\alpha}}_k &= \overline{\overline{\alpha}}_{101} = \alpha_{20}\hat{u}_y\hat{u}_y \cdot \end{aligned} \tag{A.27}$$

Using Table A.1 the explicit form of shape function α_{26} with k=3, j=3, and i=2 is

$$\alpha_{26} = L_2^2(x)L_3^2(y)L_3^2(x) = (1-x^2)\left(\frac{y(y+1)}{2}\right)\left(\frac{z(z+1)}{2}\right) \cdot \tag{A.28}$$

Similarly

$$\alpha_{16} = \left(\frac{x(x-1)}{2}\right)\left(\frac{y(y+1)}{2}\right)(1-z^2)$$
$$\alpha_{20} = (1-x^2)\left(\frac{y(y-1)}{2}\right)\left(\frac{z(z+1)}{2}\right) \quad . \tag{A.29}$$

Referring to (A.13) and substituting B for the gradient

$$\vec{\beta}_i = \vec{\beta}_{26} = \nabla\alpha_{26} = -2x\left(\frac{y(y+1)}{2}\right)\left(\frac{z(z+1)}{2}\right)\hat{i} + (1-x^2)\left(\frac{2y+1}{2}\right)\left(\frac{z(z+1)}{2}\right)\hat{j} + (1-x^2)\left(\frac{y(y+1)}{2}\right)\left(\frac{2z+1}{2}\right)\hat{k}$$
$$= \beta_{1,26}\hat{i} + \beta_{2,26}\hat{j} + \beta_{3,26}\hat{k} = \begin{bmatrix} \beta_{1,26} \\ \beta_{2,26} \\ \beta_{3,26} \end{bmatrix} \tag{A.30}$$

and

$$\vec{\beta}_j = \vec{\beta}_{16} = \nabla\alpha_{16} = \left(\frac{2x-1}{2}\right)\left(\frac{y(y+1)}{2}\right)(1-z^2)\hat{i} + \left(\frac{x(x-1)}{2}\right)\left(\frac{2y+1}{2}\right)(1-z^2)\hat{j} + \left(\frac{x(x-1)}{2}\right)\left(\frac{y(y+1)}{2}\right)(1-2z)\hat{k}$$
$$= \beta_{1,16}\hat{i} + \beta_{2,26}\hat{j} + \beta_{3,16}\hat{k} = \begin{bmatrix} \beta_{1,16} \\ \beta_{2,16} \\ \beta_{3,16} \end{bmatrix} \tag{A.31}$$

and therefore

$$\alpha_{k\ell m}\,\beta_{mj} = \alpha_{20\,\ell m}\,\beta_{m16} = \begin{bmatrix} 0 & 0 & 0 \\ 0 & \alpha_{20} & 0 \\ 0 & 0 & 0 \end{bmatrix} \times \begin{bmatrix} \beta_{1,16} \\ \beta_{2,16} \\ \beta_{3,16} \end{bmatrix} = \begin{bmatrix} 0 \\ \alpha_{20}\ \beta_{2,16} \\ 0 \end{bmatrix} \qquad \text{(A.32)}$$

Finally, substituting (A.31) and (A.32) into the integrand of (A.18)

$$\beta_{i\ell}(\alpha_{k\ell m}\beta_{mj}) = \beta_{26,\ell}(\alpha_{20\,\ell m}\beta_{m16}) = [\beta_{26,1}\ \beta_{26,2}\ \beta_{26,3}] \begin{bmatrix} 0 \\ \alpha_{20}\beta_{2,16} \\ 0 \end{bmatrix} = \beta_{26,2}\,\alpha_{20}\,\beta_{2,16} \qquad \text{(A.33)}$$

reduces (A.26) to

$$S^{*}_{26,16,101} = \int_{-1}^{1} \frac{1}{2}\,(x^6-x^5-2x^4+2x^3+x^2-x)dx \int_{-1}^{1} \frac{1}{8}\,(4y^4-3y^2-y)dy \int_{-1}^{1} \frac{1}{4}\,(-z^6+2z^3-2z^5+z^2)dz = \frac{-4}{11025} \cdot$$

(A.34)

Note that a sixth-order numerical integration scheme would be required to evaluate (A.34) exactly [45]. The remaining S* matrix entries are calculated and the entire matrix stored, preferably in core. The vector B* is obtained through a similar procedure. Table A.2 indicates storage requirements for a variety of element types.

TABLE A.2

Local Matrix S* Storage Requirements.

	Element Types			
	Homogeneous Isotropic	Inhomogeneous Isotropic	Homogeneous Orthotropic	Inhomogeneous Orthotropic
Linear 2D,n=4	(4,4,1)	(4,4,4)	(4,4,3)	(4,4,12)
Linear 3D,n=8	(8,8,1)	(8,8,8)	(8,8,6)	(8,8,48)
Quad. 2D,n=9	(9,9,1)	(9,9,9)	(9,9,3)	(9,9,27)
Quad3D n=27	(27,27,1)	(27,27,27)	(27,27,6)	(27,27,162)

A.4 THE POINT-ITERATIVE ALGORITHM

Solving (A.12) for the i'th unknown and applying (A.19) and (A.20) gives

$$\psi_i = \frac{b_i - S_{ij}\psi_j|_{i\neq j}}{S_{ii}} = \frac{B^*_{ij}f_j - S^*_{ijk}p_k\psi_j|_{i\neq j}}{S^*_{iik}p_k} \qquad (A.35)$$

which describes the field over the entire problem domain.

Although the global S* and B* matrices are exceedingly large, they are also sparse, and therefore a great deal of computational effort may be avoided by processing only those terms which contribute to the final field solution. In fact, when obtaining the solution at a particular node, only immediately adjacent elements -- nearest neighbours -- generate contributing terms to the numerator and denominator of (A.35). Because of this it is possible to work with reduced local S* and B* matrices. The algorithm flowchart is illustrated in Fig. A.2.

Initialization consists of defining the media and source characteristics and creating required local S* and B* matrices dimensioned as in Table A.2. The field is assigned a reasonable starting estimate which includes all Dirichlet boundary conditions. Note that no restriction has been placed upon intermixing of the various element types.

Once a node has been selected for processing, the algorithm determines whether or not a Dirichlet condition needs to be enforced. In a manner common to the finite difference method, such nodes are bypassed.

Local element selection involves storing the element's source, media, and field values into temporary vectors and is better understood with the aid of Fig. A.3. This enables

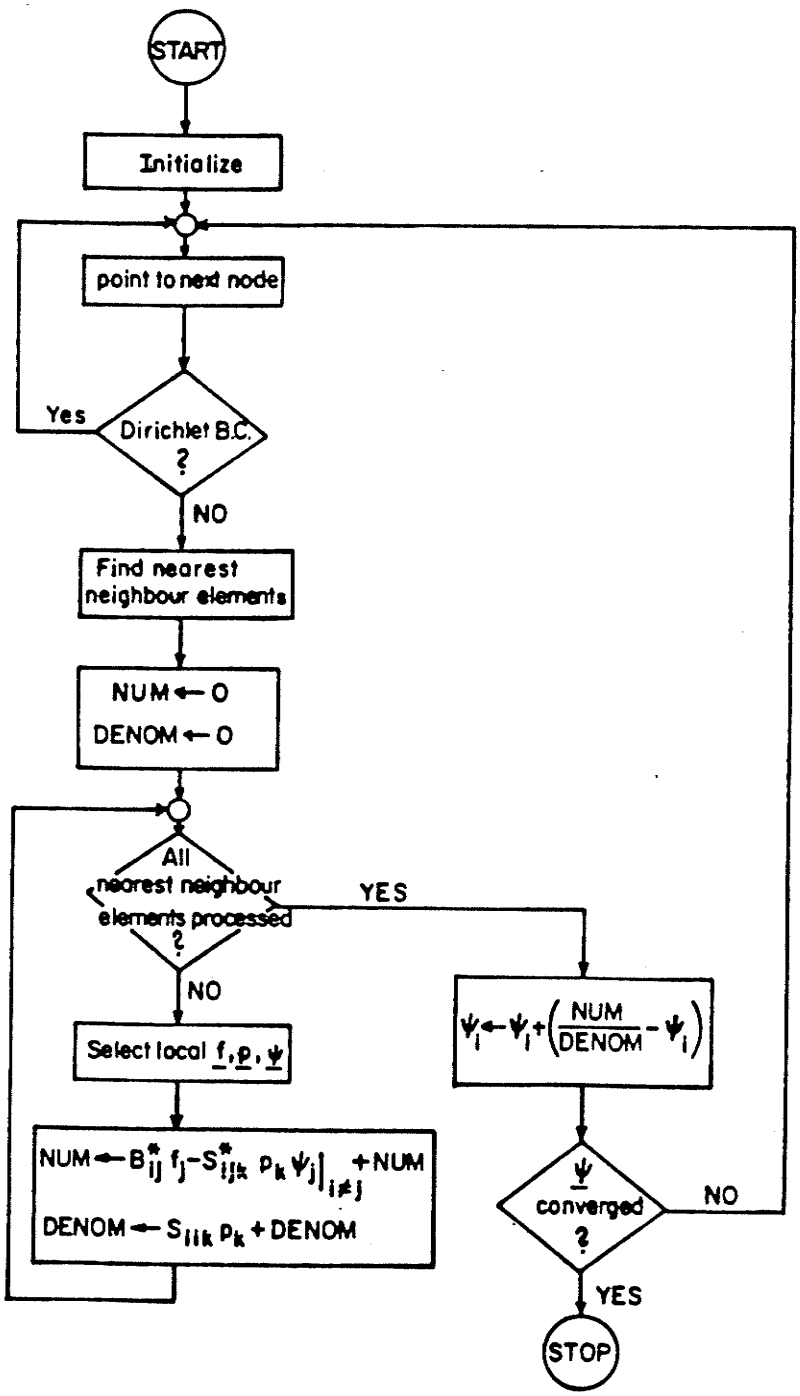

Figure A.2: Point-Iterative Algorithm Flowchart.

the calculation of the numerator and denominator contributions to proceed in a straightforward manner.

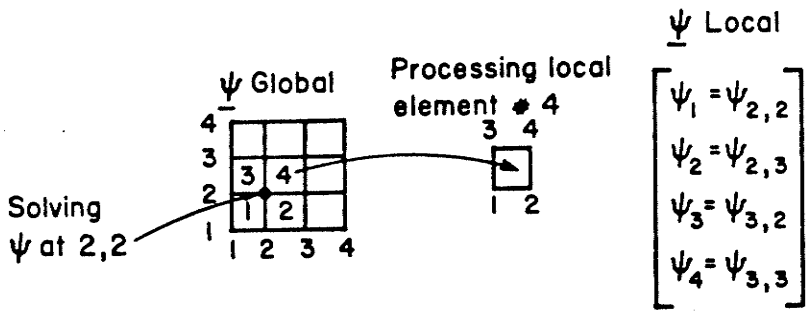

Figure A.3: Consruction of a Local Field Vector

Once all nearest neighbour elements have been processed, the estimated node potential is accelerated by standard successive overrelaxation techniques [36,46]. Iteration continues until solution has converged to the desired accuracy.

REFERENCES

1. Cohen, M., "Physics in Medical Radiology," in Physics Bulletin, October, 1975.

2. Smith, P.R., Peters, T.M., and Bates, R.H.T., "Image Reconstruction from Finite Numbers of Projections," in J. Phys. A: Math., Nucl. Gen., Vol. 6., pp. 361-381, March, 1973.

3. Brooks, R.A., and Di Chiro, G., "Principles of Computer Assisted Tomography (CAT) in Radiographic and Radioisotopic Imaging," in Phys. Med. Biol., Vol. 21, No. 5, pp. 689-732, 1976.

4. Budinger, T.F., and Gullberg, G.T., Three-Dimensional Reconstruction in Nuclear Medicine by Iterative Least-Squares and Fourier Transform Techniques. Prepared for the U.S. Atomic Energy Commission at Lawrence Berkeley Lab., University of California, UC-48 Biology and Medicine, January 1974.

5. Gordon, R., "A tutorial on ART," in IEEE Transactions on Nuclear Science, June, 1974.

6. Lewitt, R.M., Bates, R.H.T., and Peters, T.M., "Image reconstruction from projections: II:, Modified back-projection methods," in Optik, 50 (1978) No. 2, pp. 85-109.

7. Iskander, M.F. and Durney, C.H., "Electromagnetic Techniques for Medical Diagnosis: A Review," in Proceedings of The IEEE, Vol. 68, No. 1, Jan. 1980.

8. Colsher, G.J., "Fully three-dimensional positron emission tomography," in Phys. Med. Biol., Vol. 25, No. 1, pp. 103-115, 1980.

9. Budinger, T.F., Gullberg, G.T., and Huesman, R.H., "Emission Computed Tomography," in Topics in Applied Physics: Image Reconstruction from Projection, edited by Herman, G.T., Springer-Verlag: New York, pp. 147-242., 1979.

10. Shepp, L.A., "Computerized Tomography and Nuclear Magnetic Resonance," in Journal of Computer Assisted Tomography, Vol. 4, No. 1, pp. 94-107, February, 1980.

11. Hawkes, R.C., Holland, G.N., Moore, W.S., and Worthington, B.S., "Nuclear Magnetic Resonance (NMR) Tomography of the Brain: A Preliminary Clinical Assessment with Demonstration of Pathology," in Journal of Computer Assisted Tomography, Vol. 4, No. 5, pp. 577-586, October, 1980.

12. Bates, R.H.T., and McKinnon, G.C., The Inverse Problem of Ultrasonic Transmission Tomography, for the Elec. Eng. Dept., University of Canterbury, Christchurch, New Zealand.

13. Iskander, M.F., Maini, R., and Durney, C.H., "Microwave Imaging: Numerical Simulation and Results," in IEEE Trans. on M.T.T., pp. 483-484, 1981.

14. Duroux, J. and Duroux P., "Cardiopulmonary Imaging by Inductive Measurements of Electrical Conductivity," presented in St. Louis, Mo., Oct 7-9, 1976.

15. Stuchly, M. A., and Stuchly, S. S., "Dielectric Properties of Biological Substances -- Tabulated," in Journal of Microwave Power, 15(1), 1980.

16. Rush, S., Abildskov, J., and McFee, R., "Resistivity of Body Tissues at Low Frequencies," in Circulation Research, Vol. XII, Jan. 1963, pp. 40-50.

17. Geddes, L. A., and Baker, L. E., "The specific resistance of biological material - a compendium of data for the biomedical engineer and physiologist," in Medical and Biological Engineering, Vol. 5, 1967, pp. 271-293.

18. McFee, J. E., a private communication listing dielectric constants and conductivities of a wide variety of soils and rocks, Feb. 15, 1979.

19. Demers, R., Freiwald, S., and Silvester, P., "Construction of a Finite Element Model of Thorax Impedance," presented at 29th ACEMB, Nov. 6-10, 1976.

20. Fry, B., "Sensitivity of Resistance Imaging," B.Sc. Thesis for the Dept. of Elec. Eng., University of Manitoba, Winnipeg, Canada, March, 1978.

21. Witwer, J. G., Trezek, G. J., and Jewett, D. L., "The Effect of Media Inhomogenieties Upon Intracranial Electrical Fields," in IEEE Trans. on Biomedical Engineering, Vol. BME-19, No. 5, Sept., 1972.

22. Kubicek, W., Witsoe, D. and Patterson, M. "Development and Evaluation of an Impedance Cardiographic System to Measure Cardiac Output and other Cardiac Parameters," NASA, Final Progress Report, July to December, 1970.

23. Sakamoto, K., Muto, K., Kanai, H. and Lizuka, M., "Problems of Impedance Cardiography," in Med. & Biol. Eng. & Comput., November, 1979, pp. 696-709.

24. Schuler, T. and Roy, O., Potential Measuring and Display Apparatus, Especially for Electrocardiographic or Like Use, U.S. Patent # 3,294,084, Dec. 27, 1966.

25. Munro, D., Guardo, R., Bourdillon, P. and Tinker, J., "A Fourier technique for simultaneous electrocardiographic surface mapping," Cardiovascular Research, 1974.

26. Natarajan, R. and Seshadri, V., "Electric Field Distribution in the Human Body Using Finite Element Methods," in Medical and Biological Engineering, September, 1976.

27. Henderson, R. and Webster, J., "An Impedance Camera for Spatially Specific Measurements of the Thorax," in IEEE Trans. Bio. Eng., December, 1977.

28. Tasto, M. and Schomberg, H., "Object Reconstruction From Projections and Some Nonlinear Extensions," presented at NATO advanced study institute on pattern recognition and signal processing, June 25 - July 4, 1978, Paris, France.

29. Lytle, R. J. and Dines, K. A., "An Impedance Camera: A System for Determining the Spatial Variation of Electrical Conductivity," an internal report of Lawrence Livermore Laboratory, Livermore, California, Jan. 1978.

30. Telford, W. M., Geldart, L. P., Sheriff, R. E. and Keys, D. A., Applied Geophysics, Cambridge University Press, 1976, Ch. 6-8.

31. Inman, J. R., Ryu, J. and Ward, S. E., "Resistivity Inversion," in Geophysics, Vol. 38, No. 6, Dec. 1973, pp. 1088-1108.

32. Bates, R. H. T., McKinnon G. C. and Seager A. D., "A Limitation on Systems for Imaging Electrical Conductivity Distributions," in IEEE Trans. on Bio. Eng., Vol. BME-27, No. 7, July, 1980, pp. 418-420.

33. Biernacki R. M. and Bandler J. W., "Multiple-Fault Location of Analog Circuits," in IEEE Trans. on Circuits and Systems, Vol. CAS-28, No. 5, May 1981, pp. 361-367. pp. 156-160.

34. Mayeda, W. and Peponides G., "Determination of Component Values in Passive Networks Under Limited Measurements," in Proc. 12th Asimolar Conf. Circuits, Systems, and Computers, Western Periodicals, pp. 761-764, Nov. 1978. 1979, pp. 761-764.

35. Price, L. R., "Electrical Impedance Computed Tomography (ICT): A New Imaging Technique," in IEEE Trans. Nuc. Sci., Vol. NS-26, No. 2, April, 1979, pp. 2736-2739.

36. Forsythe, G.E., and Wasow, W.R., Finite-Difference Methods for Partial Differential Equations. Wiley: New York, 1960.

37. Zollenkopf, K., "Bi-Factorisation -- Basic computational algorithm and programming techniques," in Large Sparse Sets of Linear Equations, Reid, J.K. (ed.), Academic Press: New York, pp. 75-96, 1971.

38. Shaw, J., and Wexler, A., SYMPAK/ASYMPAK A Program Package for Solving Large Sparse Systems of Linear Algebraic Equations, Technical Report TR79-4, Department of Electrical Engineering, University of Manitoba, Winnipeg, Canada, 1979.

39. Wexler, A., Perspectives on the Solution of Simultaneous Equations, Technical Report TR79-2, Department of Electrical Engineering, University of Manitoba, Winnipeg, Canada, 1979.

40. Young, D.M., "Iterative solution of linear systems arising from finite element techniques," in The Mathematics of Finite Elements and Applications II, Whiteman, J.R. (ed.), Academic Press: New York, pp. 439-464, 1975.

41. Mikhlin, S.G., Variational Methods in Mathematical Physics. Pergamon Press: Oxford, 1964.

42. Harrington, R.F., Field Computation by Moment Methods. Macmillan: New York, 1968.

43. Wexler, A., "Isoparametric finite elements for continuously inhomogeneous and orthotropic media," in International Conference on Finite Elements in Water Resources Part II. Princeton University: Princeton, New Jersey, 1976.

44. Zienkiewicz, O.C., The Finite Element Method in Engineering Science. McGraw-Hill: London, 1971.

45. Stroud, A.H., and Secrest, D., Gaussian Quadrature Formulas. Prentice-Hall: Englewood Cliffs, New Jersey, 1966.

46. Varga, R.S., Matrix Iterative Analysis. Prentice-Hall: Englewood Cliffs, New Jersey, 1962.

47. Nakonechny, R., "A Sparse Linked-List Technique Using Preconditioned Conjugate Gradients For The Solution of Field Problems," M.Sc. Thesis for the Dept. of Elec. Eng., University of Manitoba, Winnipeg, Canada, May, 1983.

48. Kershaw, D.S., "The Incomplete Cholesky-Conjugate Gradient Method for the Iterative Solution of Systems of Linear Equations," Journal of Computational Physics, #26, 1978, pp. 43-65.

49. Liebeskind, D., Bases, R., Mendez, F., Elequin, F. and Koenigsberg, M., "Sister Chromatid Exchanges in Human Lymphocytes After Exposure to Diagnostic Ultrasound," Science, Vol. 205, 21 Sept., 1979, pp. 1273-1275.

50. Miller, D. L. and Nyborg, W. L., "Platelet Aggregation Induced by Ultrasound Under Specialized Conditions in vitro," Science, Vol. 205, 3 Aug., 1979, pp. 505-507.